Science Robotics
AAAS

Manuscript Template

FRONT MATTER

Title

- **Rotorigami: A Rotary Origami Protective System for Robotic Rotorcraft**

Authors

Pooya Sareh[*1,2], Pisak Chermprayong[1], Marc Emmanuelli[1], Haris Nadeem[1], Mirko Kovac[1]

*Correspondence to: pooya.sareh@liverpool.ac.uk

Affiliations

[1]Aerial Robotics Laboratory, Department of Aeronautics, Imperial College London, South Kensington Campus, SW7 2AZ, UK.

[2] Division of Industrial Design, School of Engineering, University of Liverpool, London Campus, EC2A 1AG, UK.

Abstract

Applications of aerial robots are progressively expanding in complex urban and natural environments. Despite remarkable advancements in the field, robotic rotorcraft are still drastically limited by the environment in which they operate. Obstacle detection and avoidance systems have functionality limitations and significantly add to the computational complexity of the on-board equipment of flying vehicles. Furthermore, they often cannot identify difficult to detect obstacles such as windows and wires. Robustness to physical contact with the environment is essential to mitigate these limitations and continue mission completion. However, many current mechanical impact protection concepts are either not sufficiently effective, or are too heavy and cumbersome, severely limiting the flight time as well as the capability of flying in constrained and narrow spaces. Therefore, novel impact protection systems are needed to enable flying robots to navigate in confined or heavily-cluttered environments easily, safely, and efficiently, whilst minimising the performance penalty caused by the protection method. Here, we report the development of a novel protection system for robotic rotorcraft consisting of a free-to-spin circular protector which is able to decouple impact yawing moments from the vehicle, combined with a cyclic origami impact-cushion capable of reducing the peak impact force experienced by the vehicle. Experimental results using a sensor-equipped miniature quadrotor demonstrated the impact resilience effectiveness of the Rotary Origami Protective System (Rotorigami) for a variety of collision scenarios. We anticipate this work to be a starting point for the exploitation of origami structures in the passive or active impact protection of robotic vehicles.

Summary

This paper presents a novel origami-inspired rotary protective system for improving the crash-robustness of robotic rotorcraft.

MAIN TEXT

Introduction

The emergence of rotorcraft aerial robots, popularly known as drones, offers major opportunities for applications in various areas such as environmental sensing, sampling, and surveillance. Although the potential uses of flying robots are increasing, flying in complex, constrained environments still remains a challenge. Environments with several potential collision surfaces prove to be a major limitation for unmanned aerial operations. To date, research into drone adaptation to cluttered environments has taken two different routes: (i) obstacle detection and avoidance [1-5], and (ii) mechanical impact resilience [6-18]. Conventional approaches are largely focused on obstacle avoidance using sensors to map the environment and potential collision surfaces. State of the art obstacle avoidance systems are either based on vision aided techniques [19-27] such as optical flow [28-30], or distance sensors exploiting radar [31, 32], lidar [33], and sonar [34-36] technologies. A widely used obstacle detection and avoidance method is simultaneous localisation and mapping (SLAM), which builds an accurate map of obstacles using high-precision on-board sensors [37-44]. Other effectively demonstrated methods include using collision-recovering controllers along with simple motion planners, enabling robots to navigate without complete knowledge of their surroundings. This technique allows aerial vehicles to fly in dark, GPS-denied environments [45].

Mechanical impact resilience is an alternative approach to impact protection. It seeks to cope with collisions, rather than to avoid them, which can also complement the avoidance-based methods. It is based on the fact that most conventional flying platforms are generally unable to sustain flight following a collision with a surface, as the disturbance from the impact will likely cause a loss of control and lead to a crash. Traditional drones are not equipped with any impact resilience systems, with collisions often causing failure in the major components of the vehicle. Oblique collisions will also cause an additional yawing moment around the centre of mass of the vehicle, possibly leading to instability, further collisions and crash, which generally include high impact forces and potential damage to the vehicle. Commercially available mechanical protection concepts are not sufficiently effective, and are often based on rigid components that do not mitigate collision forces. For example, propeller guards made of Expanded/Extruded Polystyrene foam (EPS/XPS) are used as a light-weight and inexpensive solution for the protection of commercial multirotor drones. However, as EPS and XPS are both rigid materials with poor elastic behavior [46, 47], they are unable to properly cushion impact forces in a recoverable manner.

Collision resilient robots aim to increase the robustness of flight operations, and can be deployed where collisions are unavoidable. Advanced mechanical concepts have been developed to tackle this problem innovatively by mitigating the translational and rotational effects of collision on the flying platform. However, in general, these concepts are heavy and cumbersome, severely limiting the flight time as well as the capability of flying in constrained and narrow spaces. As an example, Gimball [7] outstandingly reduces the impact of friction forces on the attitude of the flying platform, but imposes considerable penalties on the flight time, versatility, and transportability of the vehicle. Moreover, it does not cushion impact forces, thus normal collisions still lead to high loads on the vehicle and the colliding object.

Mitigating the impact forces in both normal and oblique collisions is a major challenge, especially for very small vehicles for which significant payload constraints prevent the

possibility of using large and heavy protective structures. Origami engineering can be a solution to address this structural design challenge. Over the past decade, origami – the traditional Japanese art of paper folding – has found numerous novel applications in various areas of robotics [48-59]. Due to the wide range of applications of origami engineering, the structural [60, 61], acoustic [62, 63], and thermal [64] properties of origami-inspired structures and metamaterials have been of great interest to scientists and engineers. For example, origami structures have been used as impact protection concepts [65-67] for potential applications such as novel crash-boxes in automotive industry [68, 69]. Furthermore, biological morphing structures such as insect and bird wings have inspired the development of origami patterns, typically finite folding patterns with a small number of vertices, as concepts for mechanical flapping wings [70-73].

In this paper, we report the design and development of a novel, lightweight, and cost-effective mechanical impact protection system for miniature quadrotor aerial platforms, and we compare it with traditional rigid propeller protection concepts. The proposed design allows these platforms to remain stable following a variety of normal and oblique collisions which are intolerable with rigid protectors. Furthermore, since collisions would become more tolerable, the proposed design could allow locomotion at potentially higher speeds, as the flight speed through complex environments can be limited due to sensing and compensation timescales. Finally, since obstacle detection becomes less crucial, the complexity and weight of the on-board sensors could potentially be reduced, significantly diminishing the computational power required.

Results

Analysis, design, and development

The principle of individual propeller guards (Fig. 1A) is currently the most common protection accessory for multicopters. Although several variations of this configuration exist (including four connected and stringed guards), the principle drawback remains the same: as the guard is fixed to the drone, the moments induced due to the arising tangential force F_t and normal force F_n will both contribute to the yawing moment about the centre of the drone which causes flight instability.

As an improvement on the common individual protectors, we aimed to develop a mechanical system that withstands collisions effectively and can be integrated into existing flying platforms. A slightly improved variation to be considered in this conceptual analysis is the decoupled individual propeller guard (Fig. 1B): if the propeller guard was to rotate independently from the drone, assuming a decoupled system is implemented, the moment arm due to F_t would be reduced. However, this configuration has the same low resilience against the yawing moment induced by the normal force as in the previous configuration.

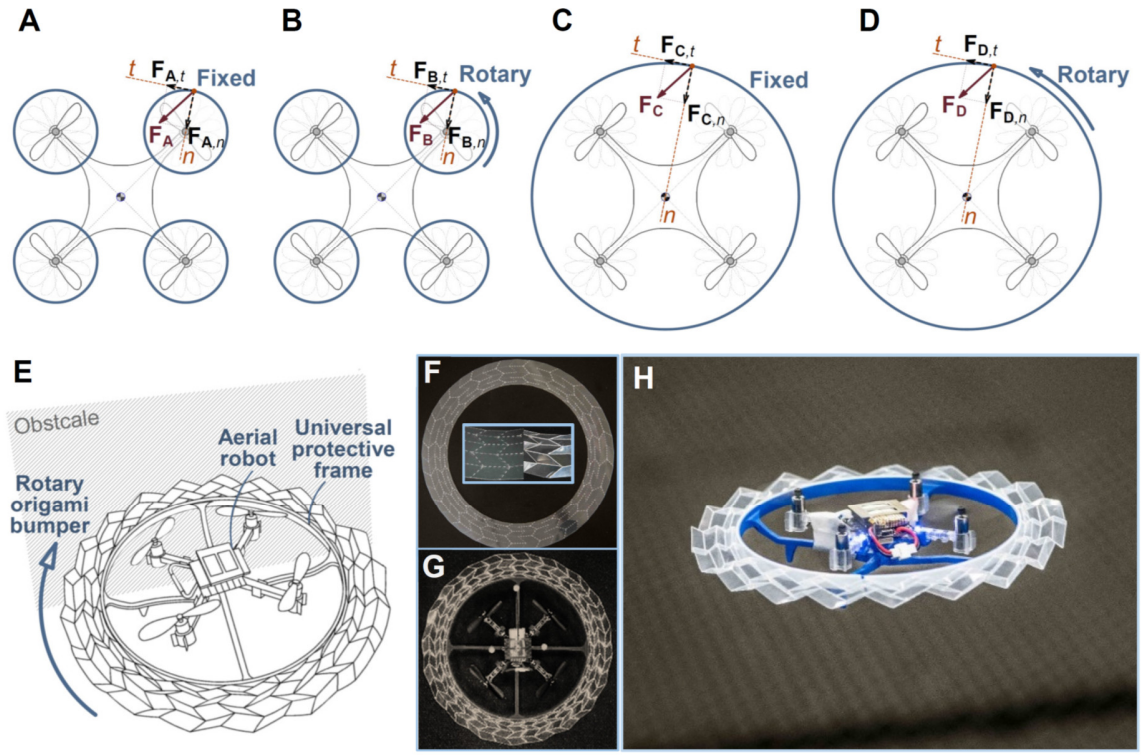

Fig. 1. Conceptual analysis, design and development of a rotary origami protective system for quadcopters. (**A** to **D**) Graphical representations of four mechanical protection systems: (**A**) Fixed individual propeller protector. (**B**) Rotary individual propeller protector. (**C**) Fixed universal protector. (**D**) Rotary universal protector. (**E**) Rotary universal protector with origami cushion. (**F**) Laser-cut pattern, and its detail view before and after folding along its perforated crease lines. (**G**) A miniature quadcopter equipped with Rotorigami (Rotary Origami Protective System) in a plan view and (**H**) in flight.

The advantage of a fixed universal (protecting all propellers) protector (Fig. 1C) over individual guards for a multicopter is that in the case of a universal guard the normal force, F_n, does not produce any yawing moment around the centre of mass of the multicopter, assuming the guard rotates around its centre of mass [8, 74]. The final and most advantageous design to be considered is a decoupled universal protector (Fig. 1D). Theoretically, assuming the centre of the universal protector is coincident with the centre of mass of the drone, and the friction in rotational joints between the platform and the protector is negligible, a decoupled universal protector will eliminate all yawing moments arising due to the collision.

In addition to moment decoupling as a first strategy, a second strategy to enhance the impact-robustness of aerial robots is to minimise the peak collision force experienced by the platform. Given the weight of protector as a main challenge, and to realise the notion of an ultra-lightweight impact cushion, we demonstrated the functionality of an origami impact protector made of a very thin plastic sheet (Fig. 1E to H). Amongst a large variety of origami patterns, the Miura-ori [75-78] is perhaps the most widely-used tessellation in engineering design, as a result of its manufacturing simplicity, geometric versatility, and desirable functional properties. In addition to free-form variations [79], several studies have proposed symmetric derivatives for this pattern which can alter both the form and functionality of the original pattern (see, e.g. [80, 81]). Variations with finite symmetry groups include several descendants with rosette symmetry (i.e. two-dimensional point groups [82]) including cyclic and dihedral descendants. Using a group-theoretic framework [83], we have designed an extensive family of isomorphic [84-86] and non-isomorphic [87, 88] wallpaper [89] symmetric variations for this pattern (Fig. 2A). While wallpaper derivatives of the pattern are useful as concepts for axial springs and crash boxes, rosette variations can be used as radial springs and shock absorbers as a result of their radial transformation. Based on a simple cyclic variation of the Miura-ori (Fig. 2B) [90-93] which allows a straightforward manufacturing process, we developed a protector capable of reducing the peak force experienced by the vehicle in a collision.

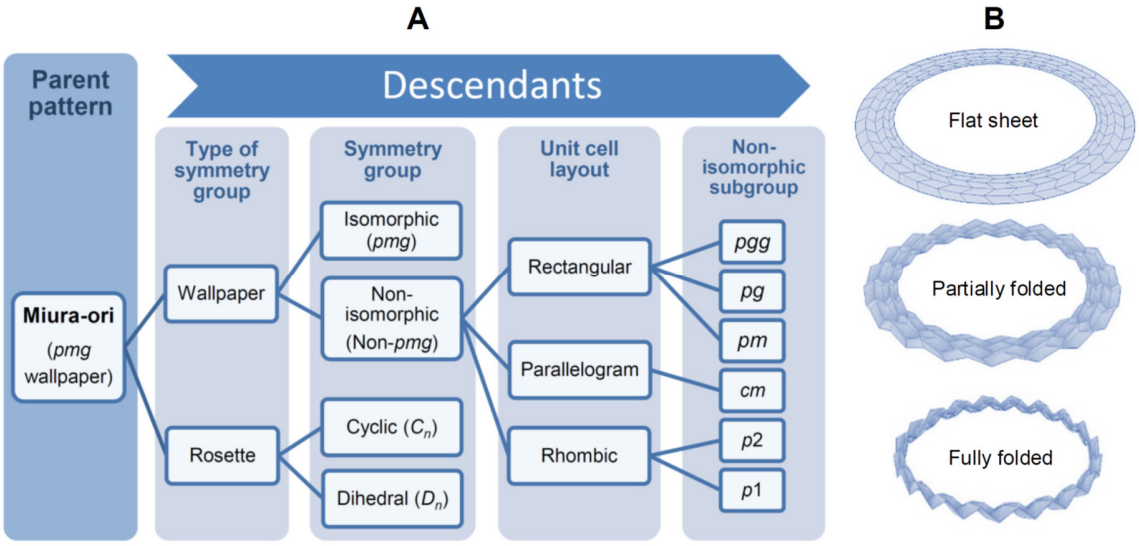

Fig. 2. Concept selection for a circular variation of the Miura-ori and its folding transformation. (A) Family tree displaying the symmetric descendants of the Miura fold pattern. **(B)** Three states in the radial transformation of a cyclic variation of the Miura-ori.

Modelling the cyclic origami ring as a function of five geometric parameters (Fig. 3A) enabled us to produce an array of different models which served as inputs to finite element analysis (FEA). The origami ring was a thin-walled structure [94], and the miniature drone was a low-speed, light-weight vehicle. As a result, in order to choose a suitable design for the ring, we adapted the quasi-static FEA simulation method which is widely used for the evaluation of impacts of thin-walled structures [95-100]. The simulations involved displacing a rigid plate towards the center of the origami structures (see Supplementary Materials for details). By performing a series of identical simulations on origami structures with varying geometric parameters, it was possible to carry out a comparative analysis, relating those parameters to the stiffness and energy absorption capabilities of the structures under compression.

The two parameters which affect the overall geometry of the structure are the number of radial segments n, and the pattern angle α, which composed a set of models to be simulated (Fig. 3C). After processing the FEA results, the structural behavior of each model was determined (for details, see section 'parametric comparative analysis of origami structures' in Supplementary Text). Specific outputs were extracted from the resulting force vs. displacement curves to characterise the structural performance of each model for the purpose of choosing a suitable design. These outputs were: (i) the elastic energy (temporarily) absorbed by the structure until it slips out of plane, (ii) the peak reaction force during compression, and (iii) the mass of the structure. It is desirable to have a lightweight protective structure with high elastic energy absorption capacity, i.e. a structure with high specific elastic energy (elastic energy per unit mass). Furthermore, in order to minimise the risk of damage to the vehicle, the protective ring must have a relatively low peak reaction force during compression.

The results showed that if the projected height of the structure H on the compressing plate is small in proportion to its width W (Fig. 3B), it will be more unstable (i.e. prone to elastic buckling). By increasing the pattern angle of the structure, it not only gets thinner (in proportion to its height), but there are also less fold lines per unit width, and the facets are each elongated in the direction of the force applied. The structure therefore becomes less stiff and more unstable. Moreover, we noticed that the energy absorbed for low pattern angles is also low (Fig. S5). In this case, the stiffness is so high that the structure slips quickly out of plane due to a high applied force before having absorbed a considerable amount of energy. Furthermore, the analyses of the stiffness and the energy absorption capabilities of the model implied that whilst increasing the number of radial segments makes the structure stiffer, it also makes it less stable. Finally, as can be seen in Fig. S7, reducing the pattern angle and increasing the number of radial segments create the most lightweight structures. The specific energy analysis (Fig. S8) indicated that, in general, a more desirable design can be achieved by choosing a pattern angle of 30°. Also, it was observed that, as a general trend, increasing the number of radial segments increases the peak reaction force.

In addition to the structural design considerations, and in order to provide a well-suited design for the intended application, we took into account the manufacturability of the structure at small scale (to suit the palm-sized flying robot used in this study) as an extra design consideration. In fact, whilst increasing n at a constant α would create a more desirable ring in terms of structural performance, it also makes the hand-folding process increasingly difficult. This is due to two reasons. Firstly, increasing n proportionally increases the number of internal vertices of the structure. This not only increases the number of lines to be folded, but makes the facets progressively smaller. Keeping in mind the limits of manual fabrication, as the facets become smaller, folding the pattern without damage to internal facets poses a substantial fabrication challenge. As a result, for the given size of the ring, we manufactured a structure with $n = 40$ as a reasonable trade-off between structural performance and manufacturability.

Based on the above mentioned considerations, we chose a suitable design with $\alpha = 30°$, $n = 40$, $r = 82.0$ mm, $m = 5$, and $w_e/w_u = 0.8$ (see the left hand side of Fig. 3D). As expected, the selected structure was observed to slip out of plane after an initial planar contraction in the FEA simulation (see the bottom part of Fig. 3D and Supplementary Materials for the simulation setup). The force vs. displacement curve (Fig. 3D) confirms this slip in the form of a sudden drop in the reaction force on the plate, after a displacement of $x = 4.33$ mm. The first derivative of this curve indicates two punctuated increases in its gradient at $x = 1.74$ mm

and $x = 2.47$ mm. These points correspond to the moments when external vertices come into contact with the plate (Fig. 3E). This triggers the facets and fold lines which are linked to these vertices to experience bending, which stiffens the structure. However, the gradient then slowly decays until the slip point. As the structure is not perfectly symmetrical about its horizontal plane, it will eventually buckle as the force imposed on it increases.

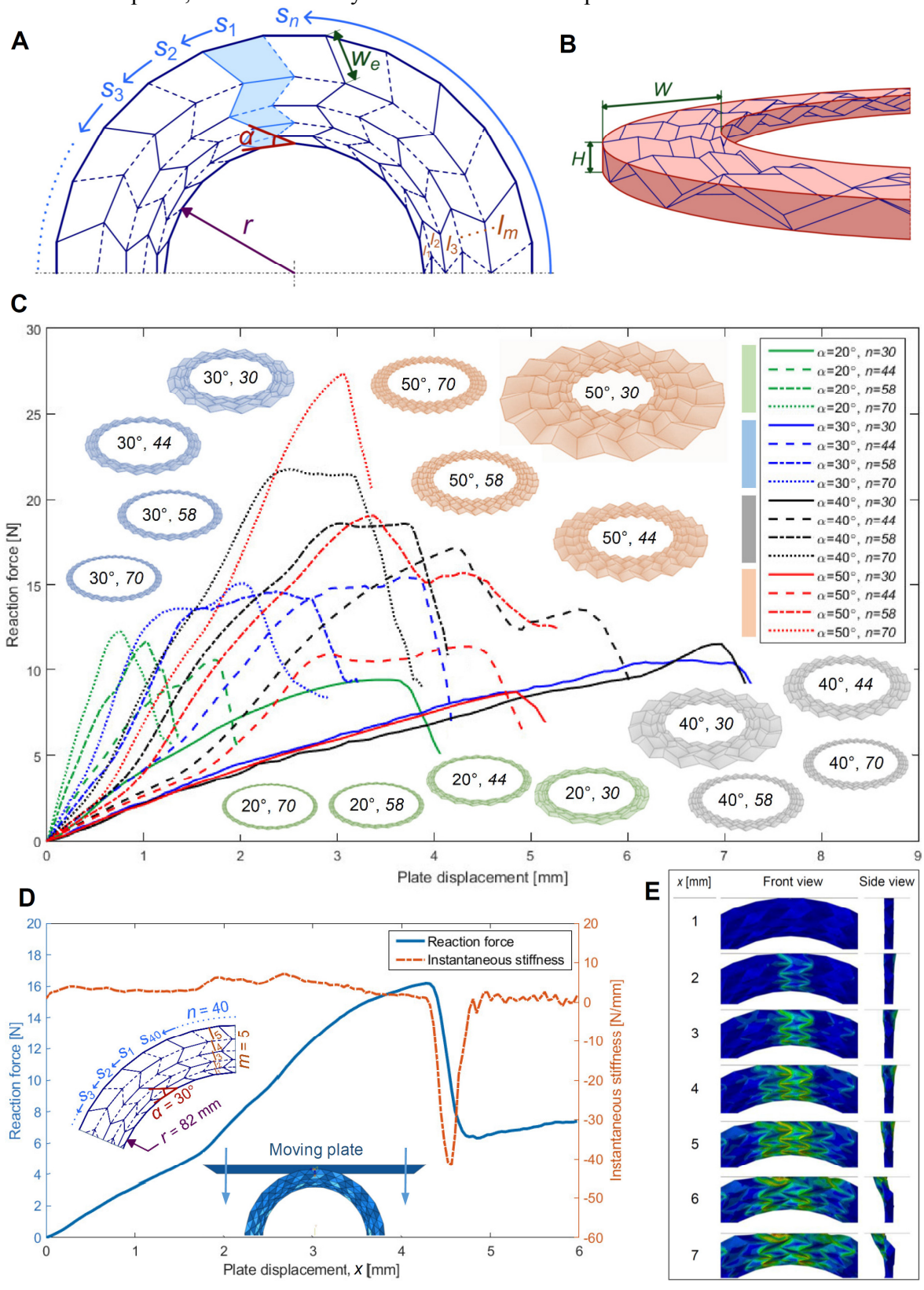

Fig. 3. Geometric modelling and structural design optimisation of the cyclic Miura-ori. (**A**) Half of a typical cyclic descendant of the Miura fold pattern and its geometric parameters: n: number of radial segments (s_1 to s_n); α: pattern angle; r: inner radius; m: number of concentric layers (l_1 to l_m); $\bar{w} = w_e / w_u$: normalised width of external facets, where w_e is the external facets width and w_u is the unchanged facets width for the pattern sequence. Mountain and valley folds are represented by solid and dashed lines, respectively. (**B**) A ring-shaped solid (mathematically speaking, a cylindrical annulus) fitting around an example model (**C**) Sixteen origami rings and output data from quasi-static FEA simulations on models with varying parameters α and n, whilst $\bar{w} = 1$. It can be seen that as the number of radial segments on the pattern is increased, so is the stiffness of the structure. However, this also has the effect of shortening the time during which the structure is stable under compression before it slips out of plane. (**D**) Reaction force vs. displacement curve for the selected design (illustrated on the left part of the figure) and its gradient which is a measure of the stiffness of the structure. The simulation setup is depicted on the bottom part of the figure (**E**) Front and side views of the FEA simulation for the compression of the selected structure.

Collision experiments and analyses

In order to investigate the capabilities of the proposed protective concept, impact experiments were carried out with a miniature multirotor aerial robot. The following are the four universal design configurations which were tested for their impact resilience performance: (i) fixed naked (Fig. 1C), (ii) rotary naked (Fig. 1D), (iii) fixed origami-protected (Fig. 1E without rotational DOF), and (iv) rotary origami-protected (Fig. 1E with rotational DOF) universal protectors. The peak impact force and angular speed of these design configurations were measured and analysed to compare their corresponding impact protection qualities in normal and oblique collisions. In these experiments, pendulum swing tests were performed using the quadcopter equipped with an IMU module as a pendulum mass. A maximum velocity of 1.2 m/s at the lowest point of the pendulum swing was set as a typical target velocity to simulate a horizontal collision to a surface. It should be mentioned that the masses of the naked and origami protector were not the same due to the added weight of the origami structure; the origami protected configurations had a mass of 53.0 g, while the naked configurations were both 48.5 g. Hence, the impact forces were calculated from the actual mass of each design configuration. The impact surfaces were switched between smooth (acrylic glass) and rough (sandpaper with ISO Grit P80) in order to determine the effect of the friction coefficient of hitting surfaces. The pendulum string held the drone at certain positions to simulate impacts at different angles of collision with respect to the colliding surface: 30°, 60°, and 90° (normal collision). For each collision scenario, the average values of force and angular speed from five tests were plotted based on 30 samples at a 600 Hz sampling frequency with peak forces aligned to show relevant force and angular speed profiles before and after the impact. Each line plot also contains its minimum and maximum values occurred in the sample datasets to show the range of the data (Fig. 4 and Fig. 5). The next two sections present the analyses of the experimental results.

Impact-cushioning strategy: naked versus origami-protected configurations

The collision duration in the origami-protected systems was observed to be significantly longer than that of the naked systems, providing a remarkable level of impact cushioning. We began by comparing the impact protection quality between the naked and origami-protected systems in a normal collision (Movie S1). The force and angular speed profiles of both systems for each experiment setup are plotted in the same figure to aid visual comparison (Fig. 4 and Table. S1). The peak force reduction turned out to be around 30% for both fixed (Fig. 4A and C) and rotary (Fig. 4B and D) origami-protected systems when compared to the naked configurations.

The next study consisted of collisions at 60º (Movie S2); given the fact that impacts at this angle are closer to normal rather than tangential collision, the normal component of the

impact force was dominant. The peak force reduction by the origami structure in both the fixed and rotary configurations was around 38% on average. Finally, for impacts at 30° with respect to the collision surface, in which the tangential collision force is dominant, the peak force reduction was around 20%.

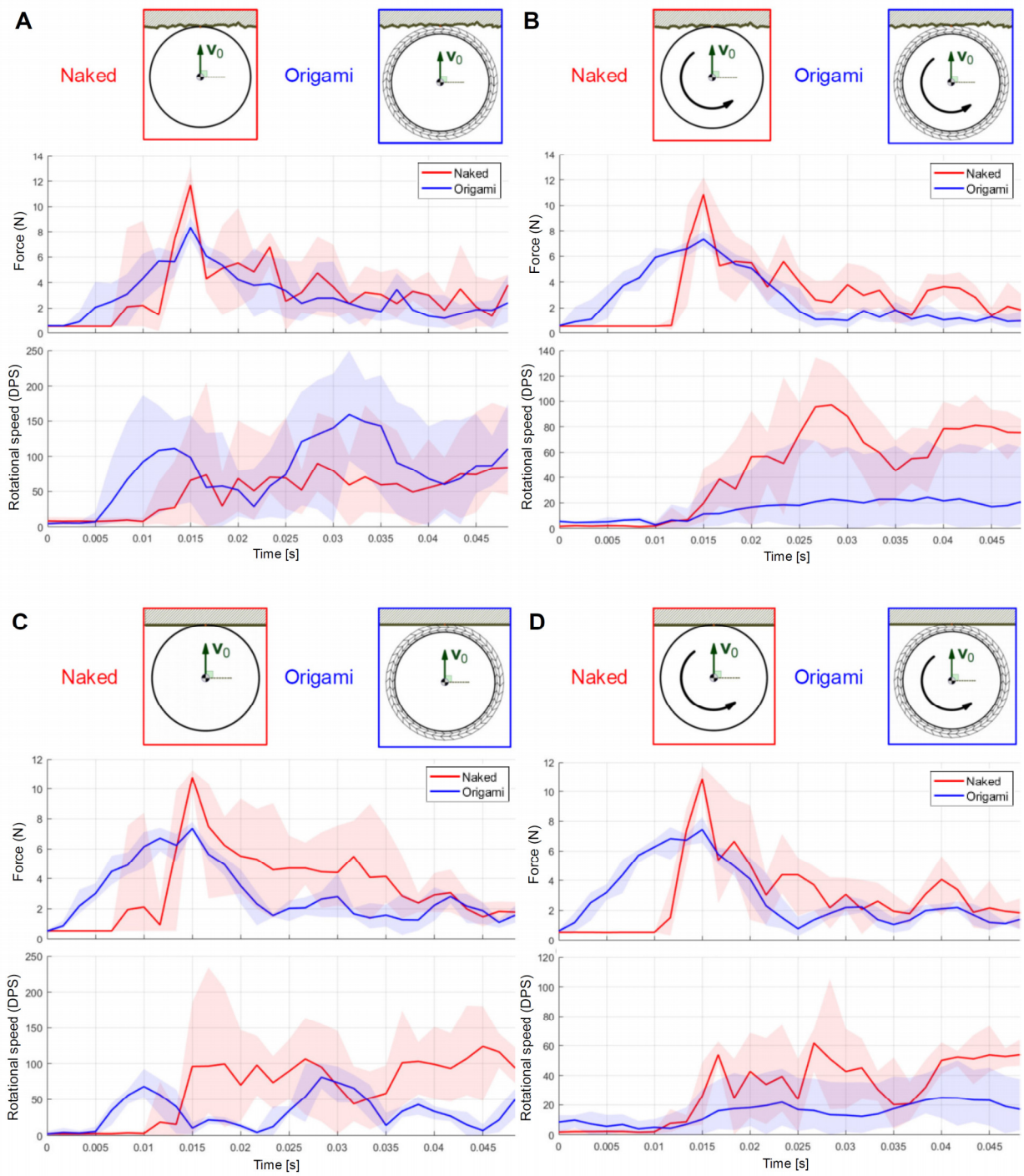

Fig. 4. Force and angular speed profiles in the normal collision (contact angle 90°) at 1.2 m/s for the naked and origami-protected configurations on the rough and smooth surfaces. The design configuration and collision conditions related to each impact scenario are illustrated by icons above each graph. The shaded areas represent the range of data (from 5 trials) corresponding to each collision. (**A**) Rough surface with fixed protector. (**B**) Rough surface with rotary protector. (**C**) Smooth surface with fixed protector. (**D**) Smooth surface with rotary protector.

Moment-decoupling strategy: fixed versus rotary configurations

In order to investigate the performance of the rotary configurations compared to the fixed ones, force and angular speed data were plotted in a way similar to the previous section. In this case, rather than comparing the naked and origami-protected systems, data for the fixed and rotary systems were plotted in the same graph for each experiment setup. The effect of the rotary concept on the reduction of rotational speed after impact was clearly demonstrated in the 30º impact experiments (Fig. 5 and Movie S3) where the tangential component of collision force was relatively large. As anticipated, every fixed protection system displayed considerably higher rotational speed after impact compared to the rotary systems. Specifically, the fixed protection systems were not effective against the rough surface in sliding collisions as the average maximum angular speed for fixed naked and fixed origami-protected systems were recorded to be around 814 and 697 degrees per second (DPS), respectively. Even though those values for the fixed protection system on the smooth surface were lower compared to those of the rough surface due to lower friction, they were still significantly high: around 392 and 579 DPS for the fixed naked and fixed origami-protected systems, respectively. On the contrary, the rotary systems effectively decoupled shear impact force, resulting in an average maximum angular speed of one order of magnitude smaller compared to those of the fixed protection systems in the collision scenarios above. In the 60º collision experiments, again the rotary protection systems showed superior impact reduction performance in all tests: it was proved that around 82% (Fig. S13 and Table S1) reduction in angular speed was achieved on average for the four collision scenarios using the moment-decoupling strategy. In normal collisions, the fixed and rotary systems performed similarly as expected due to the dominance of the normal component of the collision force (Fig. S14 and Table S1).

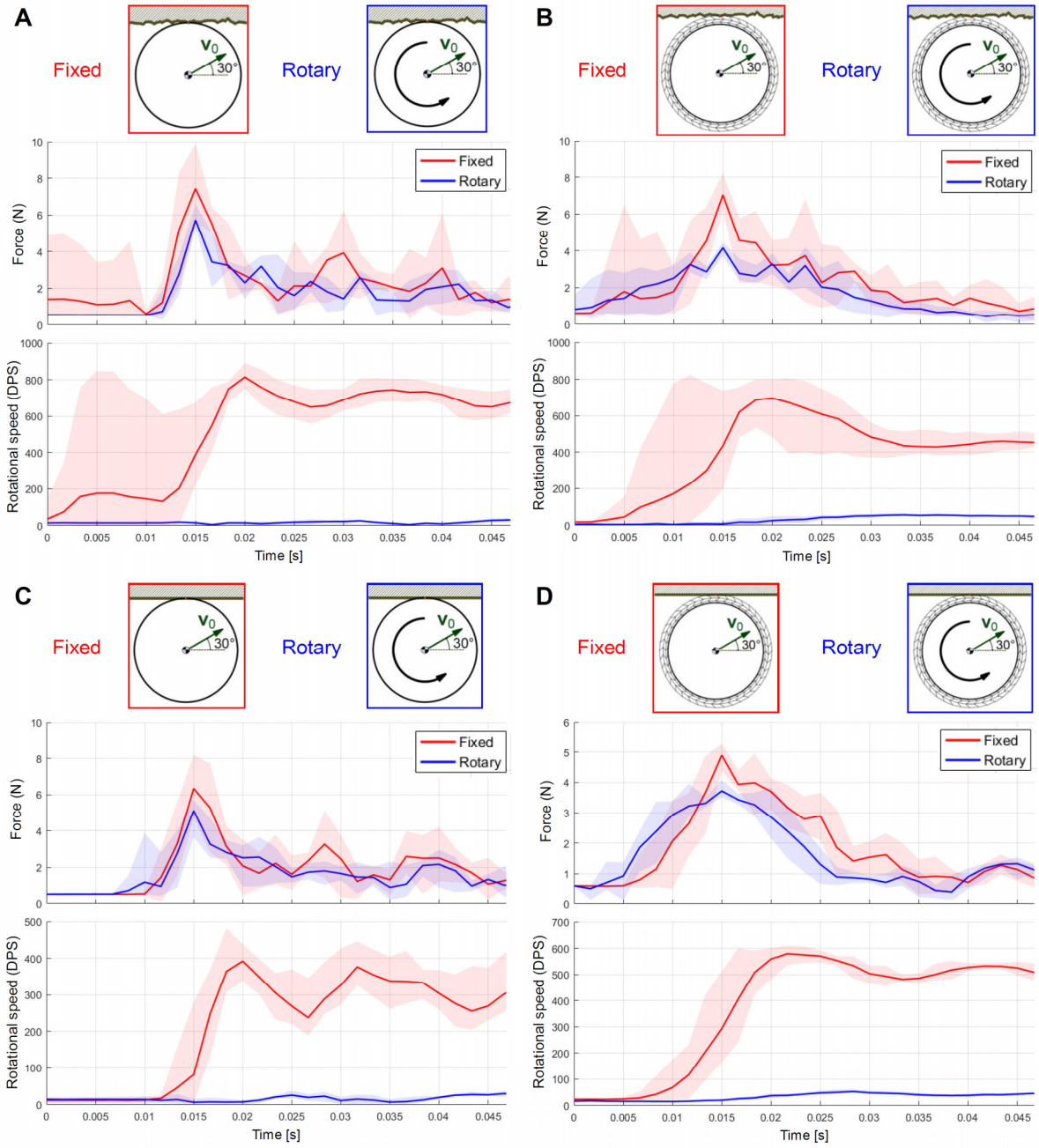

Fig. 5. Force and angular speed profiles at contact angle 30° and initial speed 1.2 m/s for the fixed and rotary configurations on the rough and smooth surfaces. The design configuration and collision conditions related to each impact scenario are illustrated by icons above each graph. The shaded areas represent the range of data (from 5 trials) corresponding to each collision. (**A**) Rough surface with naked protector. (**B**) Rough surface with origami protector. (**C**) Smooth surface with naked protector. (**D**) Smooth surface with origami protector.

Discussion

By combining a ring-shaped origami structure and a passively rotating universal circular frame, we developed and demonstrated an effective protection system that can cushion the impact to reduce the overall collision peak force experienced by the drone, as well as decouple the induced yawing moment from the platform (Fig. 6A). Extensive experimental work in a range of impact angles on both smooth and rough surfaces demonstrated that the simultaneous exploitation of these two concepts is the most advantageous design configuration in terms of the overall impact resilience quality (Fig. 6B). In summary, origami-protected systems offered approximately 30% improvement in the peak impact force reduction compared to naked-protection systems in all tested collision scenarios. By changing the material thickness and perforation settings on a laser or blade cutter, this protector can be fabricated with different levels of stiffness for diverse applications, providing a range of softness levels and therefore a range of peak force reduction capacities, appropriate for various missions and environments. For example, for low speed hovering around people and animals, or in an area with delicate and fragile obstacles, the origami ring must be scored or perforated more deeply; this provides a relatively soft protective structure that makes the vehicle safe to fly around vulnerable obstacles.

The concept motivates future research on the utility of origami structures for enhancing the impact resilience of aerial and ground robotic vehicles. Future research will also need to incorporate flight dynamic and aerodynamic studies of the proposed concept. An important note is that while the universal protective configuration remarkably improves the collision resilience of the vehicle by improving it response to the impact yawing moment, there is a pitching moment increase penalty due to the larger moment arm for the imposed out of plane component of the impact force, compared to individual protective configuration. This increased pitching moment could cause the vehicle to tip over upon contact with the obstacle in the naked configurations. However, experiments showed (Movies S1 and S4) that by equipping the vehicle with an origami ring the tendency of the vehicle to pitch is significantly decreased. This improved stability could be explained as the combination of three factors as follows: firstly, the origami ring considerably increases the mass moment of inertia of the vehicle with respect to the pitch axis; secondly, the aerodynamic resistance to pitch is larger for the origami-protected system due to its increased contact area; and finally, the peak impact force (and therefore its out of plane component) is smaller in the origami-protected configurations, leading to decreased tendency to tip over upon impact.

While this study was confined to a passive structure, it can be a start point for developing advanced concepts with actively deployable origami structures capable of adjusting their stiffness for optimal contact with different surfaces. These structures can be fully folded (retracted) when the vehicle is not flying in a cluttered environment where it experiences a higher risk of collision to obstacles. This can lead to an improved flight endurance. To enhance crash resilience, a second generation of this protective concept will include an active mechanism which protects the aerial robot in top and bottom collisions, without compromising the physical compactness of the vehicle. Furthermore, the same design principles can be extended and applied to other protected configurations such as the individual propeller guards (Fig. 6C) and universal frames with modular origami impact cushions (Fig. 6D and E). Future research will consider advanced structural concepts and further optimisation of the protective ring. This will include kirigami-inspired structures

with cut-out facets in order to decrease the structural mass of the system while preserving an appropriate level of structural performance.

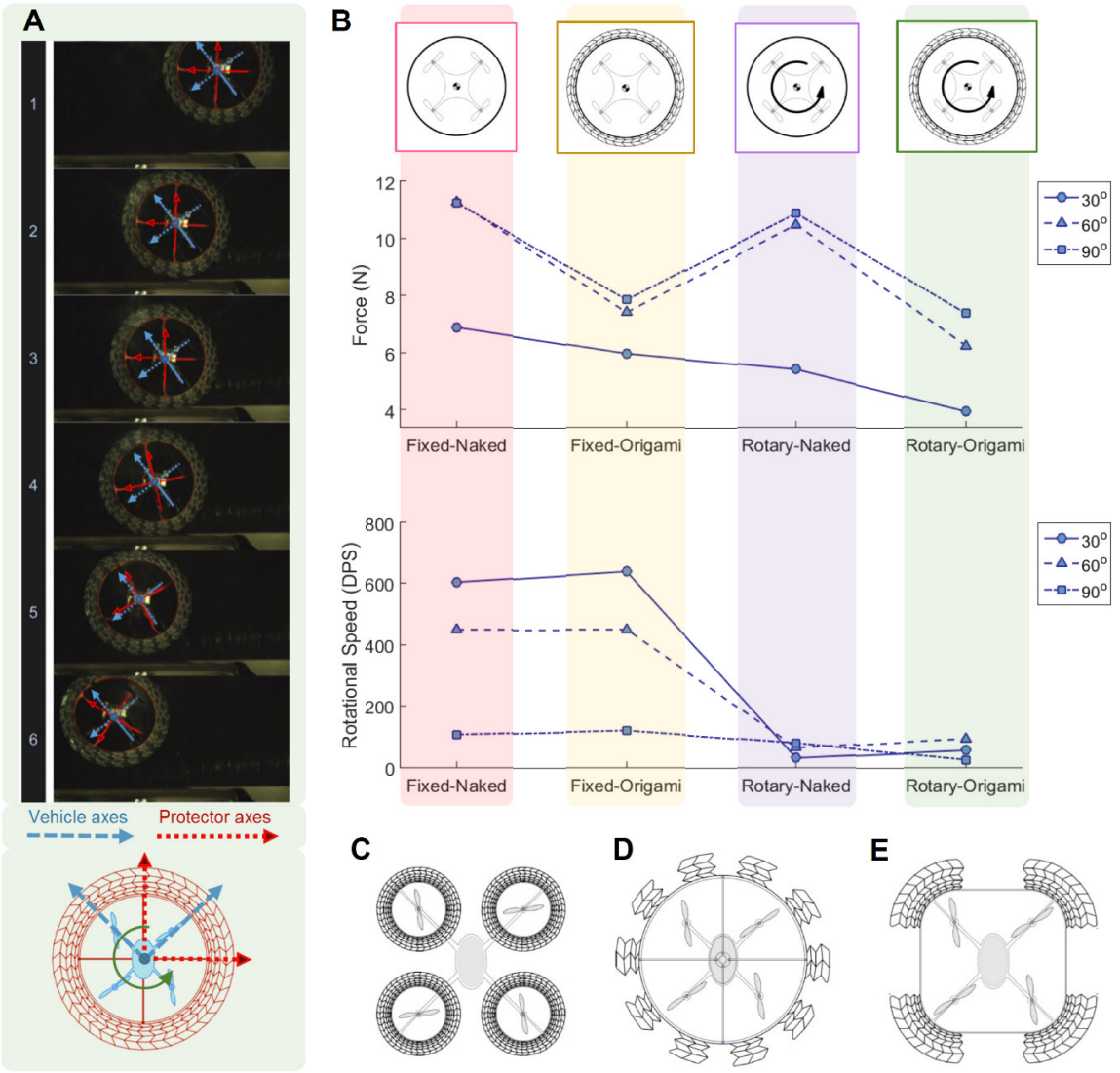

Fig. 6. Analysis of experimental results. (**A**) Snapshots from high-speed camera videos for an oblique collision to a rough surface at contact angle 30° for the origami-protected system in the the rotary configuration. As can be seen, while the protector axes (red) rotate significantly upon impact to the surface, the orientation of the vehicle body axes remains almost invariant. (**B**) Summary of all results (values averaged between rough and smooth surfaces) demonstrating that the Rotary-Origami (Rotorigami) configuration is the most advantageous design configuration in terms of the overall impact resilience quality. (**C** to **E**) A series of conceptual designs for origami-protected aerial robots.

Materials and Methods

Protective system fabrication and aerial platform selection

The impact-protection origami structure was folded manually from a 0.2 mm thick laser-cut sheet of polypropylene (Fig. 1F). To facilitate folding and to ensure the accurate geometric replication of the origami model, perforations were engraved along the fold lines of the pattern using a Versa CO_2 laser cutter (Universal Laser System PLS6.75). To change their

depth and width, these fold line perforations can be engraved using different power settings on the laser-cutter. Since low engraving power settings may create scores which do not cut through the entire thickness of the sheet, the mountain and valley fold lines were engraved separately on each side of the sheet. The plastic deformation created along the fold lines is an important element to consider when assessing the structural performance of the manufactured protection structure. The structure was assembled on a 3D-printed ABS plastic frame in the form of a cylindrical shell with a thickness of 1.1 mm. The palm-sized quadrotor Crazyflie 2.0 was chosen to be the testing platform. Its small size (92×92×29 mm) and reasonable payload capacity of up to 18 g ensured that the protection frame and origami structure were fabricated on a small scale, thereby reducing complexities in their manufacturing processes. The small size and limited payload of this platform also demonstrate the benefits of origami-inspired solutions as impact protection structures. These benefits include low weight and high design flexibility to achieve a desirable level of structural performance by perforating and folding an inexpensive plastic sheet.

Finite element simulations setup

The folded model was a three-dimensional shell object. When importing it into Abaqus Finite Element Analysis (FEA), thickness was added to it with the surface of the object as the mid-plane. This means that while the geometry of the structure was accurately represented in these models, the nature of the fold lines (with perforations and plastic deformation) was not. Perforations and plastic deformation at the fold lines reduce the stiffness of the structure, which is very difficult to accurately represent in the FEA simulations. However, the Abaqus models used in the finite element simulations were very useful for a comparative analysis to make a design decision. As this study was only concerned with horizontal impact, the simulation involved displacing a vertical rigid plate towards the center of the protection structure. For the purpose of a comparative parametric analysis, it was important to be consistent in the choice of loads and boundary constraints imposed on the structure. The origami structures were meshed using S4R shell elements. To analyse exclusively the structural behavior of the origami structure, the other components in the assembly (the quadrotor and the supportive frame) were omitted from the simulations and replaced by a rigid body constraint on the innermost vertices of the origami structure. Fig. S2B shows this constraint in Abaqus, where the vertices marked in red are parts of a fully-constrained rigid body.

Collision experiments setup and data logging system

To obtain certain collision velocities, a simple energy conservation equation between potential and kinetic energy ($E = mgh = 0.5\ mv^2$) has been used to calculate the required height at a pendulum releasing point, where E is the total amount of mechanical energy, m is the pendulum mass, h is the height of the pendulum from the releasing point to the point of impact, and v is the velocity upon impact to the wall. An electromagnet was used to hold and release the vehicle precisely to make sure that each collision has the same initial velocity and initial orientation for each testing configuration (Fig. S15A).

We integrated a miniature data logging system into the aerial robot for the measurement of dynamic variables. The MinIMU-9 V5 with LSM6DS33 (featuring a 3-axis accelerometer and a 3-axis gyroscope) and LIS3MDL (featuring a 3-axis magnetometer) was chosen as an IMU due to its small size, high data rate, and broad range of sensing. The Adafruit Feather M0 data logger with micro SD card module was programmed and connected to work with the above sensor. The connection diagram is shown in Fig. S15B. An Arduino library for

LSM6 devices from Pololu was modified using the SdFat library to increase micro SD card writing speed [101, 102]. An Ultra Micro SDHD card with UHS-I bus interface was tested with the data logger in terms of sensor data writing speed. A maximum reliable writing rate of 600 Hz was achieved with minimum and maximum time steps of 1661 and 1673 μs, respectively, between successive data samples. In order to match the above SD card data writing rate, certain LSM6 control registers were changed from default values to modify sensor ranges and data rates (see Table S2). In this configuration, the accelerometer range was set at the maximum value of ±16g and with the data rate of 833 Hz to ensure that the sampling rate was high enough so that the data logger would log a new data point from the sensor every time.

References and Notes

[1] J. Alonso-Mora, T. Naegeli, R. Siegwart, and P. Beardsley, "Collision avoidance for aerial vehicles in multi-agent scenarios," *Autonomous Robots,* vol. 39, no. 1, pp. 101-121, 2015.

[2] X. Wang, V. Yadav, and S. N. Balakrishnan, "Cooperative UAV Formation Flying With Obstacle/Collision Avoidance," *IEEE Transactions on Control Systems Technology,* vol. 15, no. 4, pp. 672-679, 2007.

[3] H. Durrant-Whyte, N. Roy, and P. Abbeel, "Unmanned Aircraft Collision Avoidance Using Continuous-State POMDPs," in *Robotics: Science and Systems VII*, Los Angeles, USA, 2012.

[4] M. T. DeGarmo, "Issues Concerning Integration of Unmanned Aerial Vehicles in Civil Airspace," MITRE Center for Advanced Aviation System Development (CAASD), McLean, Virginia2004.

[5] S. Temizer, M. J. Kochenderfer, L. P. Kaelbling, T. Lozano-Perez, and J. K. Kuchar, "Collision Avoidance for Unmanned Aircraft using Markov Decision Processes," in *AIAA Guidance, Navigation, and Control Conference*, Toronto, Canada, 2010.

[6] A. Briod, A. Klaptocz, J.-C. Zufferey, and D. Floreano, "The AirBurr: A Flying Robot That Can Exploit Collisions," in *2012 ICME International Conference on Complex Medical Engineering (CME)*, Kobe, Japan, 2012.

[7] A. Briod, P. Kornatowski, J. Zufferey, and D. Floreano, "A Collision-resilient Flying Robot," *Journal of Field Robotics,* vol. 31, no. 4, pp. 496-509, 2014.

[8] M. Kovac and P. Sareh, "Aerial Devices Capable of Controlled Flight," Patent US20180155018 (WO2016193690).

[9] M. Kovac, M. Schlegel, J.-C. Zufferey, and D. Floreano, "Steerable miniature jumping robot," *Autonomous Robots,* vol. 28, no. 3, pp. 295-306, 2010.

[10] M. Kovac, M. Schlegel, J.-C. Zufferey, and D. Floreano, "A miniature jumping robot with self-recovery capabilities," in *IEEE/RSJ International Conference on Intelligent Robots and Systems (IROS)*, St. Louis, MO, USA, 2009.

[11] M. Kovac, "The Bioinspiration Design Paradigm: A Perspective for Soft Robotics," *Soft Robotics,* vol. 1, no. 1, pp. 28-37, 2013.

[12] T. Bartelds, A. Capra, S. Hamaza, S. Stramigioli, and M. Fumagalli, "Compliant Aerial Manipulators: Toward a New Generation of Aerial Robotic Workers," *IEEE Robotics and Automation Letters,* vol. 1, no. 1, pp. 477-483, 2016.

[13] Y. Mulgaonkar, L. Guerrero-Bonilla, A. Makineni, and V. Kumar. (2016). *The Secret to Small Drone Obstacle Avoidance Is to Just Crash Into Stuff (Article by E. Ackerman)*.

[14] M. Kovac, "Learning from nature how to land aerial robots," *Science,* vol. 352, no. 6288, pp. 895-896, 2016.

[15] M. Kovac, J. Germann, C. Hürzeler, R. Y. Siegwart, and D. Floreano, "A perching mechanism for micro aerial vehicles," *Journal of Micro-Nano Mechatronics,* vol. 5, no. 3-4, pp. 77-91, 2009.
[16] Y. Mulgaonkar, T. Kientz, M. Whitzer, and V. Kumar, "Design and fabrication of safe, light-weight, flying robots," in *ASME Int. Des. Eng.Tech. Conf. Comput. Inf. Eng. Conf.*, 2015, pp. DETC 2015–47864.
[17] A. Kalantari and M. Spenko, "Modeling and Performance Assessment of the HyTAQ, a Hybrid Terrestrial/Aerial Quadrotor," *IEEE Transactions on Robotics,* vol. 30, no. 5, pp. 1278-1285, 2014.
[18] P. Kornatowski, S. Mintchev, and D. Floreano, "An origami-inspired cargo drone," in *IEEE/RSJ International Conference on Intelligent Robots and Systems (IROS)*, Vancouver, 2017.
[19] X. Yang, L. M. Alvarez, and T. Bruggemann, "A 3D Collision Avoidance Strategy for UAVs in a Non-Cooperative Environment," *Journal of Intelligent & Robotic Systems,* vol. 70, no. 1-4, pp. 315–327, 2013.
[20] E. N. Johnson, A. J. Calise, Y. Watanabe, J. Ha, and J. C. Neidhoefer, "Real-Time Vision-Based Relative Aircraft Navigation," *Journal of Aerospace Computing, Information, and Communication,* vol. 4, no. 4, pp. 707-738, 2007.
[21] G. Chowdhary, E. N. Johnson, D. Magree, A. Wu, and A. Shein, "GPS-denied Indoor and Outdoor Monocular Vision Aided Navigation and Control of Unmanned Aircraft," *Journal of Field Robotics,* vol. 30, no. 3, pp. 415–438, 2013.
[22] L. Mejias, S. McNamara, J. Lai, and J. Ford, "Vision-based detection and tracking of aerial targets for UAV collision avoidance," in *IEEE/RSJ International Conference on Intelligent Robots and Systems (IROS)*, Taipei, Taiwan, 2010.
[23] M. Odelga, P. Stegagno, and H. H. Bülthoff, "Obstacle Detection, Tracking and Avoidance for a Teleoperated UAV," in *IEEE International Conference on Robotics and Automation (ICRA)*, Stockholm, Sweden, 2016.
[24] D. Scaramuzza *et al.*, "Vision-Controlled Micro Flying Robots: From System Design to Autonomous Navigation and Mapping in GPS-Denied Environments," *IEEE Robotics and Automation Magazine,* vol. 21, no. 3, pp. 26-40, 2014.
[25] V. Kumar and N. Michael, "Opportunities and challenges with autonomous micro aerial vehicles," *The International Journal of Robotics Research,* vol. 31, no. 11, pp. 1279-1291, 2012.
[26] D. Floreano and R. J. Wood, "Science, technology and the future of small autonomous drones," *Nature,* vol. 521, pp. 460-466, 2015.
[27] R. Mahony, V. Kumar, and P. Corke, "Multirotor Aerial Vehicles: Modeling, Estimation, and Control of Quadrotor," *IEEE Robotics & Automation Magazine,* vol. 19, no. 3, pp. 20-32, 2012.
[28] J. Stowers, M. Hayes, and A. Bainbridge-Smith, "Biologically Inspired UAV Obstacle Avoidance and Control Using Monocular Optical Flow and Divergence Templates," in *International Conference on Automation, Robotics and Applications*, Wellington, New Zealand, 2011.
[29] P. C. Merrell, D.-J. Lee, and R. W. Beard, "Obstacle avoidance for unmanned air vehicles using optical flow probability distributions," in *Proc. SPIE 5609, Mobile Robots XVII*, 2004.
[30] W. E. Green and P. Y. Oh, "Optic-Flow-Based Collision Avoidance," *IEEE Robotics & Automation Magazine,* vol. 15, no. 1, pp. 96-103, 2008.
[31] Y. K. Kwag and C. H. Chung, "UAV based collision avoidance radar sensor," in *IEEE International Geoscience and Remote Sensing Symposium*, Barcelona, Spain, 2007.

[32] R. J. Fontana, E. A. Richley, A. J. Marzullo, L. C. Beard, R. W. T. Mulloy, and E. J. Knight, "An ultra wideband radar for micro air vehicle applications," in *IEEE Conference on Ultra Wideband Systems and Technologies*, Baltimore, MD, USA, 2002.
[33] R. Sabatini, M. A. Richardson, and E. Roviaro, "Development and Flight Test of an Avionics Lidar for Helicopter and UAV Low-Level Flight," *Journal of Aeronautics & Aerospace Engineering,* vol. 2, no. 3, 2013.
[34] S. Modi, P. Chandak, V. Sagar Murty, and E. L. Hall, "A Comparison of Three Obstacle Avoidance Methods for a Mobile Robot," in *Proceedings of SPIE*, 2001.
[35] N. Gageik, P. Benz, and S. Montenegro, "Obstacle Detection and Collision Avoidance for a UAV With Complementary Low-Cost Sensors," *IEEE Access,* vol. 3, pp. 599-609, 2015.
[36] J. F. Roberts, T. S. Stirling, J.-C. Zufferey, and D. Floreano, "Quadrotor Using Minimal Sensing For Autonomous Indoor Flight," in *European Micro Air Vehicle Conference and Flight Competition (EMAV2007)*, Toulouse, France, 2007.
[37] A. Bachrach, R. He, and N. Roy, "Efficient Planning under Uncertainty for a Target-Tracking Micro-Aerial Vehicle," in *Proceedings of the 28th International Conference on Machine Learning*, Bellevue, WA, USA, 2011.
[38] S. Shen, N. Michael, and V. Kumar, "Autonomous Multi-Floor Indoor Navigation with a Computationally Constrained MAV," in *IEEE International Conference on Robotics and Automation*, Shanghai, 2011.
[39] M. Blosch, S. Weiss, D. Scaramuzza, and R. Siegwart, "Vision Based MAV Navigation in Unknown and Unstructured Environments," in *IEEE International Conference on Robotics and Automation*, Anchorage, AK, USA, 2010.
[40] J. M. M. Montiel, J. Civera, and A. J. Davison, "Unified Inverse Depth Parametrization for Monocular SLAM," in *Robotics: Science and Systems*, Philadelphia, Pennsylvania, 2006.
[41] D. Magree, J. G. Mooney, and E. N. Johnson, "Monocular visual mapping for obstacle avoidance on UAVs," in *International Conference on Unmanned Aircraft Systems (ICUAS)*, Atlanta, GA, USA, 2013.
[42] S. Weiss, D. Scaramuzza, and R. Siegwart, "Monocular-SLAM–based navigation for autonomous micro helicopters in GPS-denied environments," *Journal of Field Robotics,* vol. 28, no. 6, pp. 854-874, 2011.
[43] M. W. Achtelik, S. Lynen, S. Weiss, L. Kneip, M. Chli, and R. Siegwart, "Visual-inertial SLAM for a small helicopter in large outdoor environments," in *IEEE/RSJ International Conference on Intelligent Robots and Systems (IROS)*, 2012.
[44] L. Doitsidis, A. Renzaglia, S. Weiss, E. Kosmatopoulos, D. Scaramuzza, and R. Siegwart, "3d surveillance coverage using maps extracted by a monocular slam algorithm," in *IEEE/RSJ International Conference on Intelligent Robots and Systems (IROS)*, 2011.
[45] Y. Mulgaonkar, A. Makineni, L. Guerrero-Bonilla, and V. Kumar, "Robust Aerial Robot Swarms Without Collision Avoidance," *IEEE Robotics and Automation Letters,* vol. 3, no. 1, pp. 596-603, 2018.
[46] L. J. Gibson and M. F. Ashby, *Cellular Solids: Structure and Properties (Cambridge Solid State Science Series)*. Cambridge University Press, 1999.
[47] S. Mcvicker. (2017). *Shear Wall Basics (http://www.mcvicker.com/vwall/page003.htm)*.
[48] S. Felton, M. Tolley, E. Demaine, D. Rus, and R. J. Wood, "A method for building self-folding machines," *Science,* vol. 345 no. 6197, pp. 644-646, 2014.
[49] C. D. Onal, M. T. Tolley, R. J. Wood, and D. Rus, "Origami-Inspired Printed Robots," *IEEE/ASME Transactions on Mechatronics* vol. 20, no. 5, 2015.
[50] J. Paik, "Reconfigurable materials: Algorithm for architectural origami," *Nature,* vol. 541, pp. 296–297, 2017.
[51] S. Miyashita, S. Guitron, S. Li, and D. Rus, "Robotic metamorphosis by origami exoskeletons," *Science Robotics,* vol. 2, no. 10, 2017.

[52] E. V. Hoff, D. Jeong, and K. Lee, "OrigamiBot-I: A thread-actuated origami robot for manipulation and locomotion," in *IEEE/RSJ International Conference on Intelligent Robots and Systems (IROS)*, Chicago, IL, USA, 2014.
[53] L. Dae-Young, K. Sa-Reum, K. Ji-Suk, P. Jae-Jun, and C. Kyu-Jin, "Origami Wheel Transformer: A Variable-Diameter Wheel Drive Robot Using an Origami Structure," *Soft Robotics,* vol. 4, no. 2, pp. 163-180, 2017.
[54] J. Mu, C. Hou, H. Wang, Y. Li, Q. Zhang, and M. Zhu, "Origami-inspired active graphene-based paper for programmable instant self-folding walking devices," *Science Advances,* vol. 1, no. 10, 2015.
[55] L. Paez, G. Agarwal, and J. Paik, "Design and Analysis of a Soft Pneumatic Actuator with Origami Shell Reinforcement," *Soft Robotics,* vol. 3, no. 3, 2016.
[56] D. S. Rus, Cynthia "Spotlight on origami robots," *Science Robotics,* vol. 3, no. 15, 2018.
[57] A. Z. Rafsanjani, Yuerou; Liu, Bangyuan; Rubinstein, Shmuel M.; Bertoldi, Katia, "Kirigami skins make a simple soft actuator crawl," *Science Robotics,* vol. 3, no. 15, 2018.
[58] S.-J. Kim, D.-Y. Lee, G.-P. Jung, and K.-J. Cho, "An origami-inspired, self-locking robotic arm that can be folded flat," *Science Robotics,* vol. 3, no. 16, 2018.
[59] S. Mintchev, J. Shintake, and D. Floreano, "Bioinspired dual-stiffness origami," *Science Robotics,* vol. 3, no. 20, 2018.
[60] C. Lv, D. Krishnaraju, G. Konjevod, H. Yu, and H. Jiang, "Origami based Mechanical Metamaterials," *Scientific Reports,* vol. 4, p. 5979 2014.
[61] J. T. B. Overvelde *et al.*, "A three-dimensional actuated origami-inspired transformable metamaterial with multiple degrees of freedom," *Nature Communications,* vol. 7, p. 10929, 2016.
[62] S. Babaee, J. T. B. Overvelde, E. R. Chen, V. Tournat, and K. Bertoldi, "Reconfigurable origami-inspired acoustic waveguides," *Science Advances,* vol. 2, no. 11, p. e1601019, 2016.
[63] R. L. Harne and D. T. Lynd, "Origami acoustics: using principles of folding structural acoustics for simple and large focusing of sound energy," *Smart Materials and Structures,* vol. 25, no. 8, p. 085031, 2016.
[64] R. B. Mulford, M. R. Jones, and B. D. Iverson, "Dynamic Control of Radiative Surface Properties With Origami-Inspired Design," *Journal of Heat Transfer,* vol. 138, no. 3, pp. HT-15-1128, 2016.
[65] W. Wu and Z. You, "Energy absorption of thin-walled tubes with origami patterns," in *5th International Meeting on Origami in Science, Mathematics and Education (5OSME)*, Singapore, 2010.
[66] J. Song, Y. Chen, and G. Lu, "Axial crushing of thin-walled structures with origami patterns," *Thin-Walled Structures,* vol. 54, pp. 65-71, 2012.
[67] S. H. Min C.C., "Geometrical Properties of Paper Spring," in *Manufacturing Systems and Technologies for the New Frontier. Springer, London*, 2008.
[68] J. Ma and Z. You, "Energy Absorption of Thin-Walled Square Tubes With a Prefolded Origami Pattern—Part I: Geometry and Numerical Simulation," *Journal of Applied Mechanics,* vol. 81, no. 1, 2014.
[69] K. Terada, K. Kadoi, S. Tokura, T. Sushida, and I. Hagiwara, "The deformation mechanism on origami-based foldable structures," *International Journal of Vehicle Performance,* vol. 3, no. 4, pp. 334–346, 2017.
[70] F. Haas and R. J. Wootton, "Two Basic Mechanisms in Insect Wing Folding," *Proceedings of the Royal Society B: Biological Sciences,* vol. 263, no. 1377, pp. 1651-1658, 1996.
[71] F. Haas, "Wing Folding in Insects: A Natural, Deployable Structure," in *IUTAM-IASS Symposium on Deployable Structures: Theory and Applications*, Cambridge, UK, 2000.

[72] A. K. Stowers and D. Lentink, "Folding in and out: passive morphing in flapping wings," *Bioinspiration & Biomimetics,* vol. 10, p. 025001, 2015.
[73] L. Dufour, K. Owen, S. Mintchev, and D. Floreano, "A drone with insect-inspired folding wings," in *IEEE/RSJ International Conference on Intelligent Robots and Systems (IROS)*, Daejeon, South Korea, 2016
[74] P. Sareh, P. Chermprayong, M. Emmanuelli, H. Nadeem, and M. Kovac, "The Spinning Cyclic 'Miura-oRing' for Mechanical Collision-Resilience," in *The 7th International Meeting on Origami in Science, Mathematics and Education (7OSME)* Oxford, UK, 2018.
[75] K. Miura, "Map Fold a La Miura Style, Its Physical Characteristics and Application to the Space Science," *Research of Pattern Formation, edited by R. Takaki, KTK Scientific Publishers,* pp. 77-90, 1994.
[76] K. Miura, "The Science of Miura-ori: A Review," in *Fourth International Conference on Origami in Science, Mathematics, and Education (4OSME)*, Pasadena, CA, 2006: Fourth International Conference on Origami in Science, Mathematics, and Education (4OSME).
[77] P. Sareh, "Symmetric Descendants of the Miura-ori," *PhD Dissertation, Engineering Department, University of Cambridge, UK,* 2014.
[78] K. Miura, "Method of Packaging and Deployment of Large Membranes in Space," *The Institute of Space and Astronautical Science report,* no. 618, pp. 1-9, 1985.
[79] T. Tachi, "Generalization of Rigid-Foldable Quadrilateral-Mesh Origami," Valencia, Spain, 2009: Proceedings of the International Association for Shell and Spatial Structures (IASS).
[80] Y. Klett and K. Drechsler, "Designing Technical Tessellations," in *5th International Meeting on Origami in Science, Mathematics and Education (5OSME)*, Singapore, 2010.
[81] R. J. Lang and A. Bateman, "Every Spider Web has a Simple Flat Twist Tessellation," in *5th International Meeting on Origami in Science, Mathematics and Education (5OSME)*, Singapore, 2010.
[82] T. Hahn, *International Tables for Crystallography, Volume A: Space-group symmetry*. USA: Springer, 2005.
[83] P. Sareh and S. D. Guest, "A Framework for the Symmetric Generalisation of the Miura-ori," *International Journal of Space Structures, Special Issue on Folds and Structures,* 2015.
[84] P. Sareh and S. D. Guest, "Minimal Isomorphic Symmetric Variations on the Miura Fold Pattern," in *The First International Conference on Transformable Architecture (Transformable 2013)*, Seville, Spain, 2013.
[85] P. Sareh and S. D. Guest, "Designing symmetric derivatives of the Miura-ori," *Advances in Architectural Geometry,* pp. 233-241, 2014.
[86] P. Sareh and S. D. Guest, "Design of Isomorphic Symmetric Descendants of the Miura-ori," *Smart Materials and Structures,* vol. 24, no. 8, p. 085001, 2015.
[87] P. Sareh and S. D. Guest, "Tessellating Variations on the Miura Fold Pattern," in *IASS-APCS Symposium*, Seoul, South Korea, 2012.
[88] P. Sareh and S. D. Guest, "Design of non-isomorphic symmetric descendants of the Miura-ori," *Smart Materials and Structures,* vol. 24, no. 8, p. 085002, 2015.
[89] R. L. E. Schwarzenberger, "The 17 plane symmetry groups " *Mathematical Gazette 58,* pp. 123-131, 1974.
[90] P. T. Barreto, "Lines meeting on a surface: The "MARS" paperfolding," in *Origami Science & Art: Proceedings of the Second International Meeting of Origami Science and Scientific Origami*, Otsu, Japan, 1997, pp. 343–359.
[91] T. Nojima, "Modelling of Folding Patterns in Flat Membranes and Cylinders by Origami," *JSME International Journal Series C,* vol. 45, no. 1, pp. 364-370, 2002.
[92] T. Hull, R. Lang, and R. Schamp, "Pleated Multi-sliced Cone," in *The 2012 Joint Mathematics Meetings*, Boston, USA, 2012.

[93] R. J. Lang, "Oval Tessellation," ed: http://www.langorigami.com/crease-pattern/oval-tessellation.
[94] M. Bischoff, K. U. Bletzinger, W. Wall, and E. Ramm, "Models and Finite Elements for Thin-Walled Structures," in *Encyclopedia of computational mechanics*: John Wiley & Sons, Ltd, 2004.
[95] G. Lu and T. Yu, *Energy absorption of structures and materials*. Woodhead Publishing Ltd and CRC Press LLC, 2003.
[96] A. G. Mamalis and W. Johnson, "The quasi-static crumpling of thin-walled circular cylinders and frusta under axial compression," *International Journal of Mechanical Sciences,* vol. 25, no. 9-10, pp. 713-732, 1983.
[97] W. Johnson, *Crashworthiness of Vehicles*. Institution of Mechanical Engineers, 1978.
[98] L. Zheng and T. Wierzbicki, "Quasi-static crushing of S-shaped aluminum front rail," *International Journal of Crashworthiness,* vol. 9, no. 2, pp. 155-173, 2004.
[99] T. Borvik, O. S. Hopperstad, A. Reyes, M. Langseth, G. Solomos, and T. Dyngeland, "Empty and foam-filled circular aluminium tubes subjected to axial and oblique quasistatic loading," *International Journal of Crashworthiness,* vol. 8, no. 5, pp. 481- 494, 2003.
[100] N. Jones, *Structural Impact*. Cambridge University Press, 1997.
[101] *https://github.com/pololu/lsm6-arduino*.
[102] *https://github.com/greiman/SdFat*.
[103] Simulia, Abaqus Analysis User's Manual (Abaqus 6.12), Simulia Corp., Providence, RI, USA, 2012.

Acknowledgments, Funding, Author contributions, Competing Interests and Data and materials availability can be found in the formated version at: http://robotics.sciencemag.org/content/3/22/eaah5228?rss=1

SUPPLEMENTARY MATERIALS

Supplementary Text

Fig. S1. Estimation of the inner diameter of a fully-folded cyclic Miura-ori ring. The inner diameter of the fully-folded origami ring is a function of pattern angle and the number of radial segments.

Fig. S2. Finite Elements simulations setup. (A) Finite Elements simulation setup for compression test. (B) Rigid body constraint on vertices marked in red.

Fig. S3. Top view of a model displaying the angles between successive external vertices.

Fig. S4. Stiffness of each model in the parametric matrix.

Fig. S5. Energy absorbed by each model in the parametric matrix.

Fig. S6. Ratio of height to width of each model in the parametric matrix.

Fig. S7. Mass of each model in the parametric matrix.

Fig. S8. Specific energy for each model in the parametric matrix.

Fig. S9. Peak reaction force for each model in the parametric matrix.

Fig. S10. Effect of the width of the most external facets (parameter E). (A) Array of models with external facet of varying width. (B) Numerical output of reference model with varying external facet width.

Fig. S11. Force and angular speed profiles at contact angle 60° for naked and origami protected configuration on rough and smooth surfaces. (A) Impact on rough surface with fixed protector. (B) Impact on rough surface with rotary protector. (C) Impact on smooth surface with fixed protector. (D) Impact on smooth surface with rotary protector.

Fig. S12. Force and angular speed profiles at contact angle 30° for naked and origami protected configuration on rough and smooth surfaces. (A) Impact on rough surface with fixed protector. (B) Impact on rough surface with rotary protector. (C) Impact on smooth surface with fixed protector. (D) Impact on smooth surface with rotary protector.

Fig. S13. Force and angular speed profiles at contact angle 60° for fixed and rotary configuration on rough and smooth surfaces. (A) Impact on rough surface with naked protector. (B) Impact on rough surface with origami protector. (C) Impact on smooth surface with naked protector. (D) Impact on smooth surface with origami protector.

Fig. S14. Force and angular speed profiles at contact angle 90° for fixed and rotary configuration on rough and smooth surfaces. (A) Impact on rough surface with naked protector. (B) Impact on rough surface with origami protector. (C) Impact on smooth surface with naked protector. (D) Impact on smooth surface with origami protector.

Fig. S15. (A) Experimental setup for pendulum collision tests of a miniature quadcopter to a surface. (B) Connection between MinIMU-9 V5 and Adafruit Feather M0 data logger.

Fig. S16. (A) Drawing for mountain fold lines perforations (blue). (B) Drawing for valley fold lines perforations (blue) and the borders of the ring to be cut (red). (C) Laser perforation and cutting of the origami pattern from a polypropylene sheet (including perforation and cutting settings). (D) Manual folding process of the perforated pattern with plastic deformation along the fold lines during fabrication. (E) A quarter of the pattern folded manually. (F) Components of the rotary origami protective system including the circular frame (ABS), connector/bearing housing (ABS), shaft (aluminum), bearing (steel), and origami bumper (polypropylene).

Table S1. Summary of experimental results.

Table S2. Control registers for the IMU.

Movie S1. Oblique collision to a rough surface at contact angle 30º for the origami-protected and naked systems in the fixed and rotary configurations at 1.2 m/s (0.03x).

Movie S2. Oblique collision to a rough surface at contact angle 60º for the origami-protected and naked systems in the fixed and rotary configurations at 1.2 m/s (0.03x).

Movie S3. Normal collision to a rough surface for the origami-protected and naked systems in the fixed and rotary configurations at 1.2 m/s (0.03x).

Movie S4. Normal collision to a rough surface for the origami-protected system in the fixed and rotary configurations at 2 m/s (0.03x), and collisions of the aerial vehicle in the Rotorigami configuration with different obstacles during flight demonstrations.

Supplementary Materials for

Rotorigami: A Rotary Origami Protective System for Robotic Rotorcraft

Pooya Sareh*, Pisak Chermprayong, Marc Emmanuelli, Haris Nadeem, Mirko Kovac

*Correspondence to: pooya.sareh@liverpool.ac.uk

This PDF file includes:

Supplementary Text
Figs. S1 to S16
Tables S1 to S2
Captions for Movies S1 to S4

Other Supplementary Materials for this manuscript includes the following:

Movies S1 to S4

Supplementary Text

Parametric modelling of the origami structure

The five parameters which fully define the cyclic origami pattern (Fig. 3A) are:

A. *Number of radial segments* (*n*): This is the number of segments into which the circle is divided. It has to be an even number to keep the number of mountain and valley fold lines equal. In this model, it ranges from 30º to 70º.

B. *Pattern angle* (α): Changing one angle will affect all others as there is only one degree of freedom dictating all angles in this origami pattern. In this model, we decided to change the acute angle of the most internal facets from 20º to 50º.

C. *Inner diameter* (*r*): The inner diameter shrinks as the origami ring is folded. An empirical function was established from folding simulations using the software Freeform Origami. We estimated the suitable inner diameter of the two-dimensional pattern in order for the folded structure to fit around the circular protective frame of the drone.

D. *Number of concentric layers* (*m*): For simplicity and to focus on continuous parameters, this value was held constant at 5 in our model, and we did not investigate the effects of varying this parameter on structural performance.

E. *Width of external facets* (w_e): The width of facets on the external edge of the pattern provides an extra degree of freedom. This parameter, w_e, is expressed as a factor of the unchanged facet width w_u, i.e., $\bar{w} = w_e / w_u$, where w_e is the external facet width and w_u is the unchanged facet width in the pattern sequence. In this study, the normalised width $\bar{w}$ was set to range from 0.6 to 1.4.

Fig. 2B shows a cyclic Miura-ori fold pattern in three different folding states. The diameter of the structure shrinks as it is folded. The extent at which the inner diameter shrinks was computationally evaluated for a series of different models. It is found to depend on both the number of radial segments (parameter *A*) and the pattern angle (parameter *B*). Using curve fitting, it was possible to establish a mathematical function relating the extent at which the inner diameter of the structure shrinks to these two initial geometric parameters (Fig. S1). As a result, the diameter of the fully folded origami structures can be estimated for any set of parameters. The numerical details of this analysis can be found in Appendix A. The naturally folded state is the relaxed partially folded state (Fig. 2B) in which the origami structure remains after it has been folded by hand and endured plastic deformation along its fold lines. It has a complex dependency on the manufacturing process, notably on the degree of plastic deformation along the fold lines and the fatigue endured by the structure after multiple impact tests. It is important to know the value which the inner diameter of the two-dimensional origami pattern needs to have for the naturally folded origami to be assembled on a certain circular frame. Knowing the diameter of the fully folded model from the empirical relation enabled us to measure the diameter of the origami structure to be manufactured. Considering the small range of initial geometric parameters used, we assumed the following linear relation is valid for all set of parameters:

$$\frac{\text{Inner diameter}_{\text{flat sheet}} - \text{Inner diameter}_{\text{naturally folded}}}{\text{Inner diameter}_{\text{flat sheet}} - \text{Inner diameter}_{\text{fully folded}}} = \text{constant}$$

This formula, together with the empirical function relating the geometric parameters to the diameter of the fully folded model, can be inserted in the parametric model to eliminate one parameter, the diameter of the pattern, leaving us with three variables defining the geometry of our model.

Parametric comparative analysis of origami structures

The two parameters which affect the overall geometry of the structure (n, the number of radial segments, and α, the pattern angle) composed a set of models to be simulated (Fig. 3C). As parameter E ($\bar{w}$, the normalized width of external facets) has a more singular effect on the structural behavior of the model, it would compose a simple array of models which all have the reference values for parameters A and B. Fig. 3C also shows the output data from 16 simulations on models with varying parameters A and B. It is clear that as the number of radial segments on the pattern is increased, so is the stiffness of the structure. However, this also has the effect of shortening the time during which the structure is stable under compression before it slips out of plane. The stiffness gradient for each model under compression experiences an increase as external vertices become in contact with the plate. To illustrate this phenomenon, Fig. S3 shows a top view of a model displaying the angles between successive external vertices. As the number of radial segments is increased, the angles between successive lines decrease proportionally, and more external facets will be in contact with a compressing plate for a given displacement. Consequently, more fold line will be solicited to contribute to supporting the applied force and stiffness will increase.

Fig. S4 shows the average elastic gradients measured for each curve in the range of force between zero and 5 N. Using the MATLAB Basic Fitting tool, these 16 measurements can serve as a baseline to empirically estimate the stiffness a model with any initial geometric parameters. It is clear from these measurements that the number of radial segments has a direct effect on the stiffness for the reasons explained above. However, we also notice that decreasing the pattern angle increases the stiffness. Indeed, doing so creates a more compact structure, as the number of fold lines is maintained but the width of the structure decreases. As a consequence, facets are less likely to experience local buckling as their projected length in the direction of the compressive load is reduced. The next output parameter to consider in the prospect of choosing a suitable design is the energy temporarily absorbed by the origami structure (the area under the force vs. displacement curve) until it slips out of plane in the case of frictionless contact (Fig. S5). This is also a measure of the stability of the structure under compression. For the same reason as the stiffness of the model being low, the energy absorbed is low if the pattern angle is too high. To illustrate this, Fig. 3B shows a ring-shaped solid fitting around the origami model. This ring can be fully defined according to its height and width. Fig. S6 shows the ratio of these two measurements.

The last design consideration is the mass of the structure, which is obtained from measuring the surface of the origami pattern and multiplying it by the thickness of the sheet and the density of polypropylene. As can be seen in Fig. S7, reducing the pattern angle and increasing the number of radial segments creates the most lightweight structures (less than

5 grams). Again, these curves can be extrapolated to formulate a function providing the mass of models of any geometry. This information, as well as the projected width of the structure, are important ingredients to consider in the prospect of possible future studies on the aerodynamics and fight stability of the assembly.

An energy absorption analysis (Fig. S8) indicated that, in general (strictly speaking, in all cases except when the number of radial segments is 70), a better energy-absorbing design can be achieved by choosing a pattern angle of 30°. The peak reaction force for each model is depicted in Fig. S9.

Apart from the number of radial segments (parameter *A*) and the pattern angle (parameter *B*), we mentioned another geometric variable being the width of the most external facets (parameter *E*). The array of models in Fig. S10A were simulated to give the results displayed in Fig. S10B.

The loss in stiffness and total energy absorbed by the larger models confirms the fact that elongating facets in the direction of the applied force creates local buckling which weakens the structure. This phenomenon is observed for models with the external facets width exceeding the normal width for the pattern sequence. For widths below this reference value, the force vs. displacement curves are comparable to each other, as the facets are short enough not to buckle.

For the purpose of our comparative analysis on parametric origami models, we chose to consistently use the frictionless case as it pin points a clear moment at which the structure becomes unstable. Indeed, the fact that there is no threshold for friction force means that the first local instability will trigger the whole structure to slip out of plane. The simulations involved displacing a rigid plate at a constant speed of 5 mm/s towards the center of the origami structures. This loading rate ensured a quasi-static analysis as recommended in [103].

Experimental comparison between naked and origami protective systems

Experimental results comparing naked and origami for 60° and 30° collisions are presented in Fig. S10 and Fig. S11, respectively. The comparisons between the fixed and rotary concepts for 60° and 90° collisions are given in Fig. S13 and Fig. S14, respectively.

Laser cutting and perforation settings

Fig. S16A and B show the 2D drawings to be sent to the Versa CO_2 laser cutter. Note that the valley fold lines are perforated on the reverse side of the sheet. Fig. S16C depicts the origami ring perforated and cut from a thin polypropylene sheet using the laser cutter (including perforation and cutting settings). Fig. S16D depicts the manual folding process of the perforated pattern with plastic deformation along the fold lines during fabrication. Fig. S16E shows a quarter of the folded pattern. Fig. S16F represents the components of the rotary origami protective system including the circular frame (ABS), connector/bearing housing (ABS), shaft (aluminum), bearing (steel), and origami bumper (polypropylene).

Appendix A. Estimation of maximum diameter shrink

x = parameter A: number of strips ; y = parameter B: pattern angle [degrees]

Measurements of diameter shrink of fully-folded origami [mm]

x	y					
	20	30	40	50	60	70
20	1,71	6,53	14,22			
30	2,90	8,59	17,08	27,35	41,10	
40	3,59	9,71	18,58	30,26	43,26	
50	4,04	10,41	19,51	31,42	44,78	59,53
60	4,38	10,89	20,13	31,89	45,49	61,12
70	4,57	11,19	20,66	32,07	46,20	61,34
80	4,71	11,43	20,93	32,68	46,61	61,92

Maximum diameter shrink: $z = ay^2 + by + c$.

$a = p_1x^4 + q_1x^3 + r_1x^2 + s_1x + t_1$,

$b = p_2x^4 + q_2x^3 + r_2x^2 + s_2x + t_2$,

$c = p_3x^4 + q_3x^3 + r_3x^2 + s_3x + t_3$.

where p_i, q_i, r_i, s_i, and t_i (i =1, 2, 3) are given in the following table.

	p	q	r	s	t
1	-1.63×10^{-9}	2.97×10^{-7}	-1.68×10^{-5}	2.34×10^{-4}	-1.42×10^{-2}
2	1.65×10^{-7}	-3.00×10^{-5}	-1.69×10^{-3}	-2.23×10^{-2}	-2.52×10^{-1}
3	-3.53×10^{-6}	-6.76×10^{-4}	-4.29×10^{-2}	-9.51×10^{-1}	-5.99

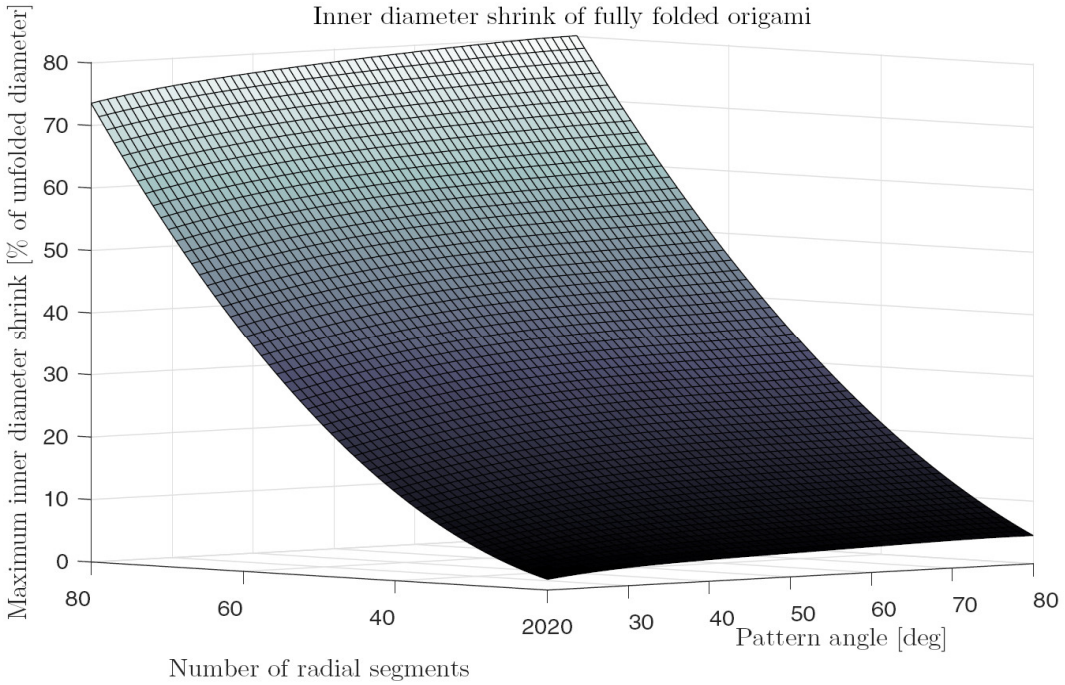

Fig. S1. Estimation of the inner diameter of a fully-folded cyclic Miura-ori ring. The inner diameter of the fully-folded origami ring is a function of pattern angle and the number of radial segments.

A

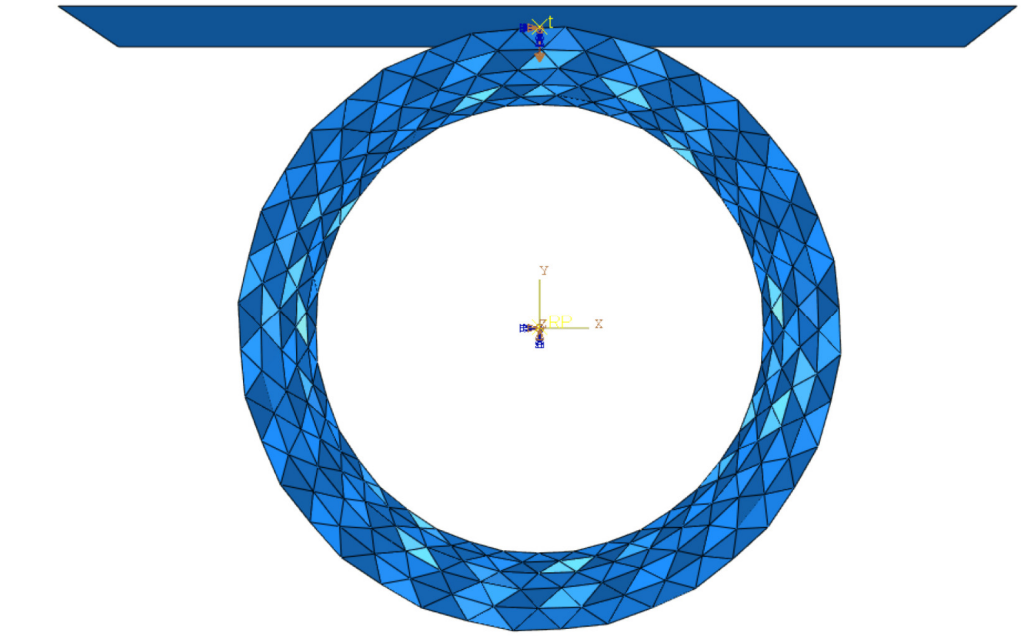

B

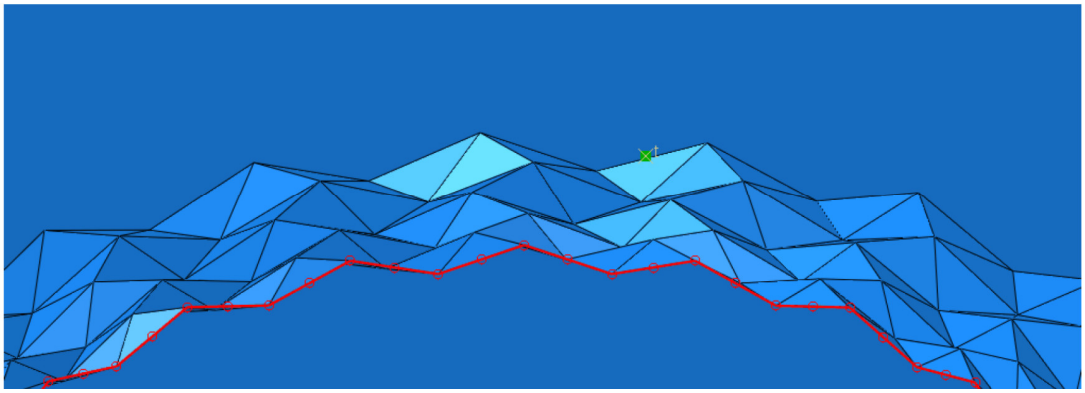

Fig. S2. (A) Finite element simulation setup for compression test. (B) Rigid body constraint on vertices marked in red.

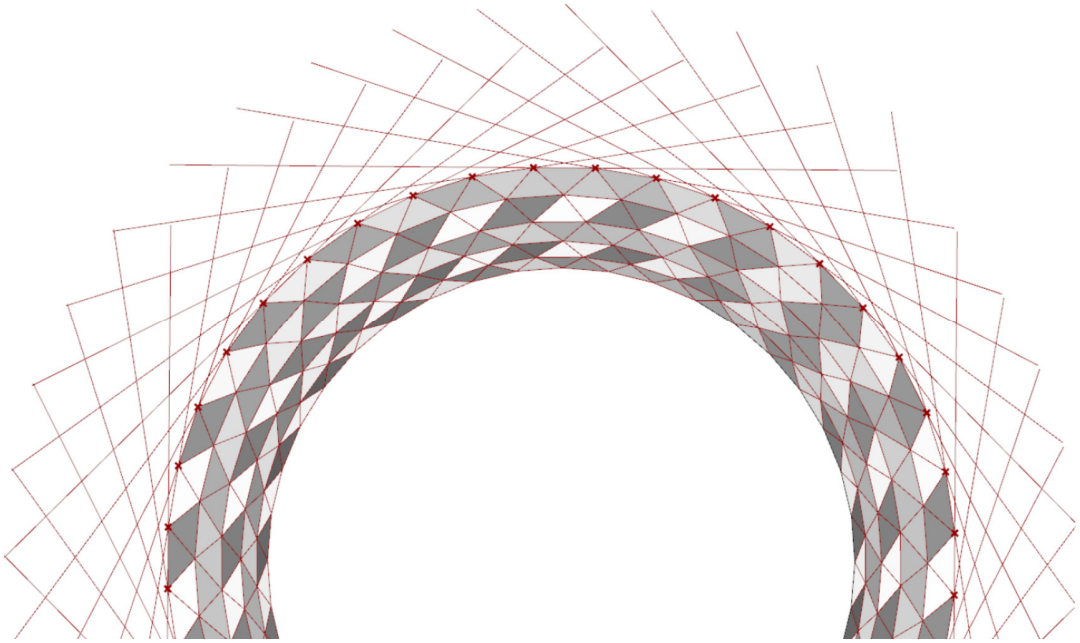

Fig. S3. Top view of a model displaying the angles between successive external vertices

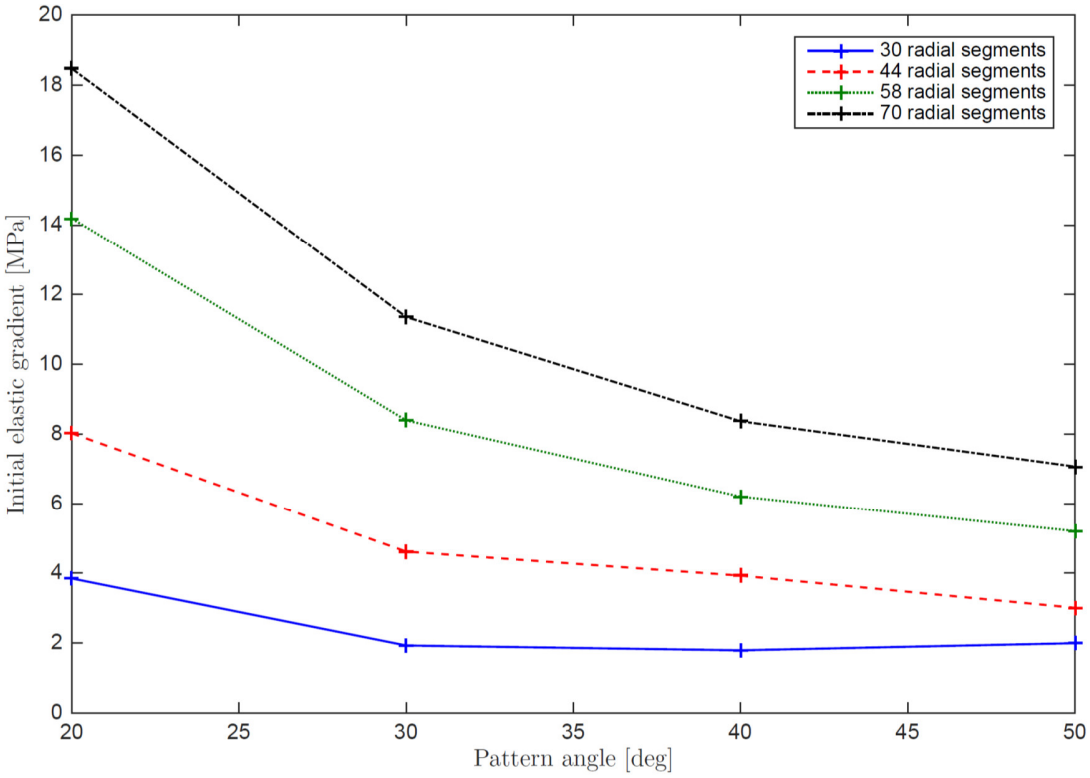

Fig. S4. Stiffness of each model in the parametric matrix

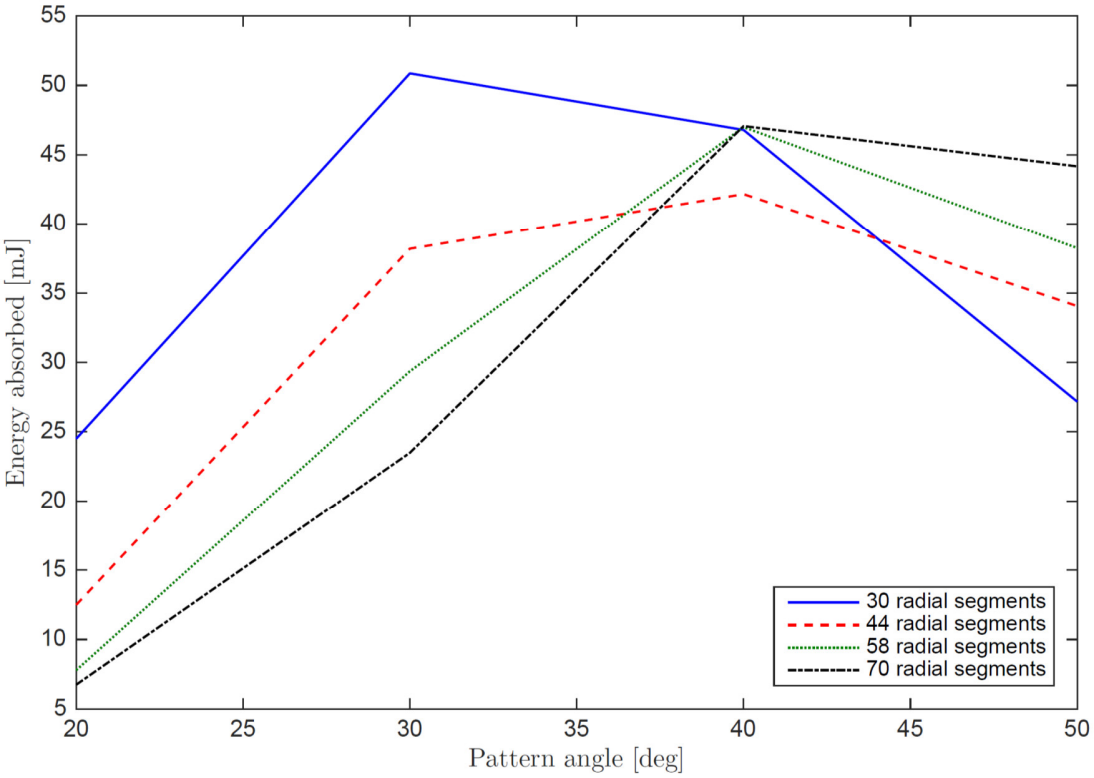

Fig. S5. Energy absorbed by each model in the parametric matrix until the structure slips out of plane

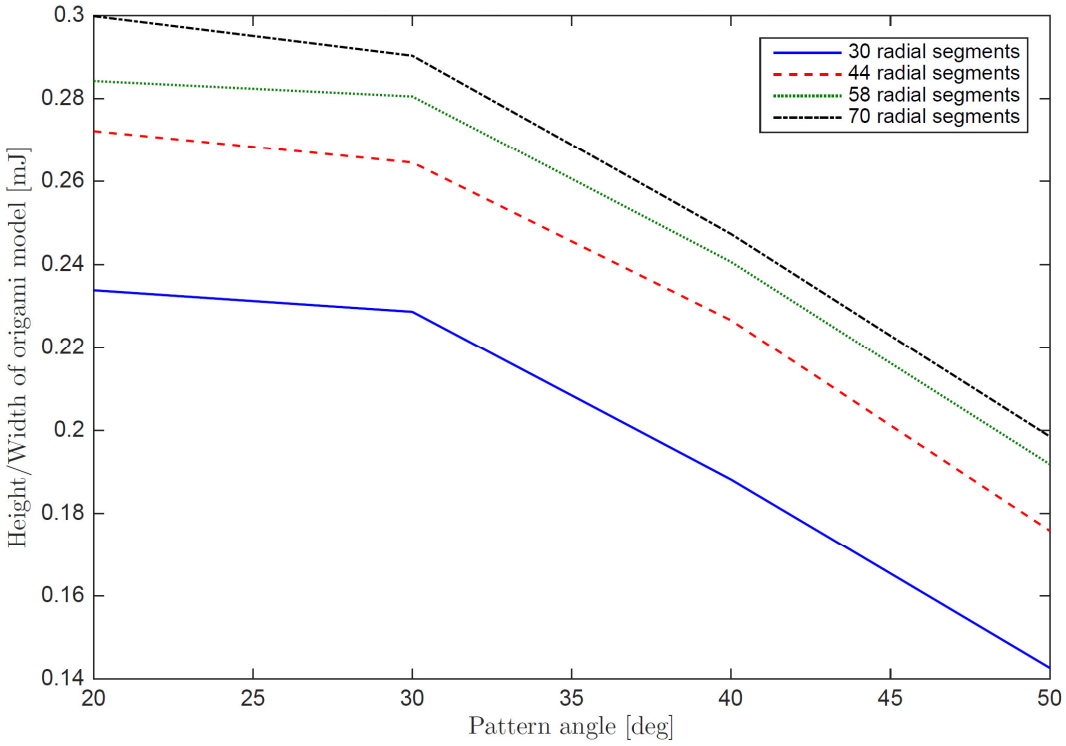

Fig. S6. Ratio of height to width for each model in the parametric matrix

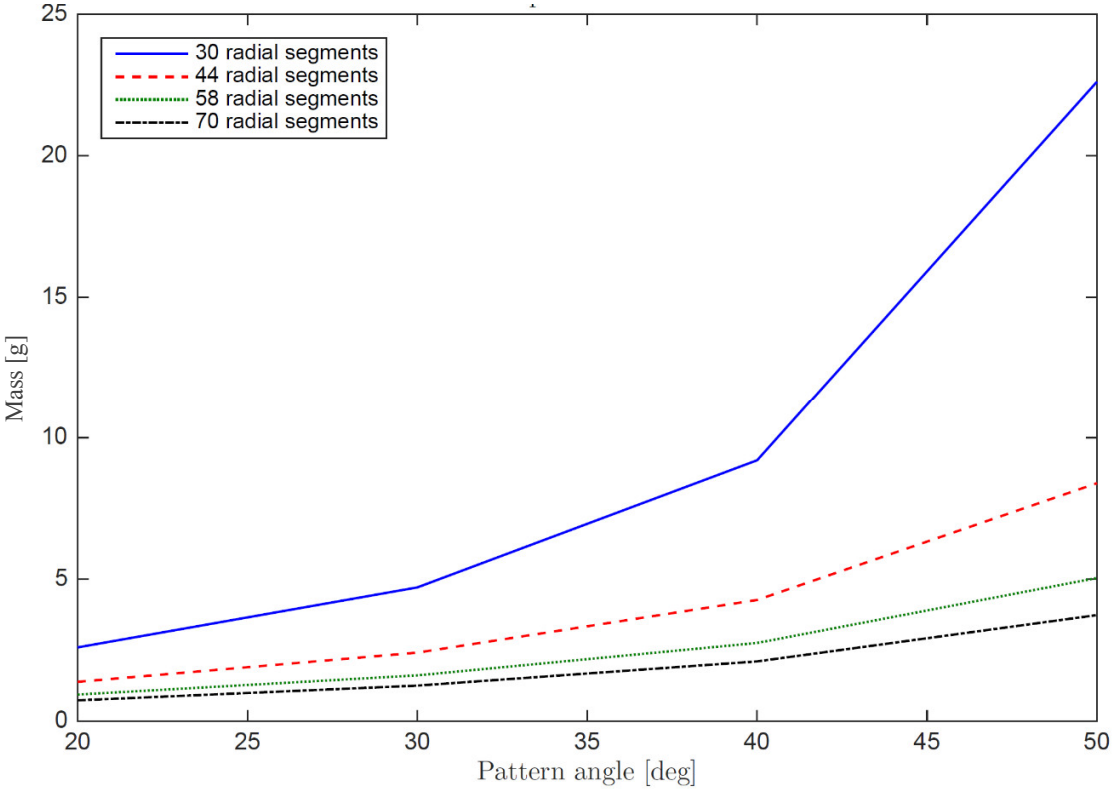

Fig. S7. Mass of each model in the parametric matrix

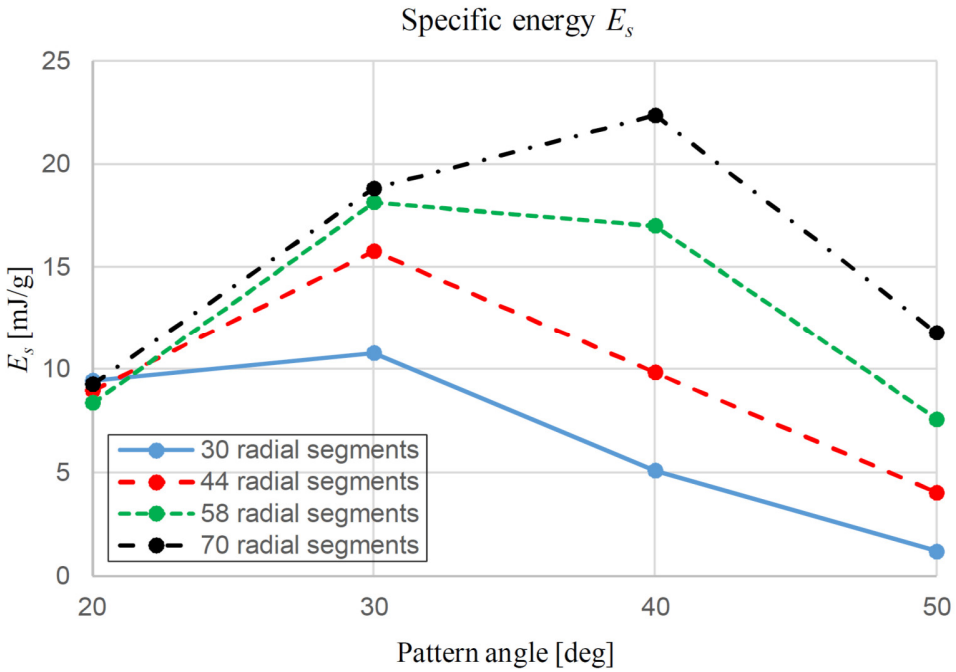

Fig. S8. Specific energy for each model in the parametric matrix

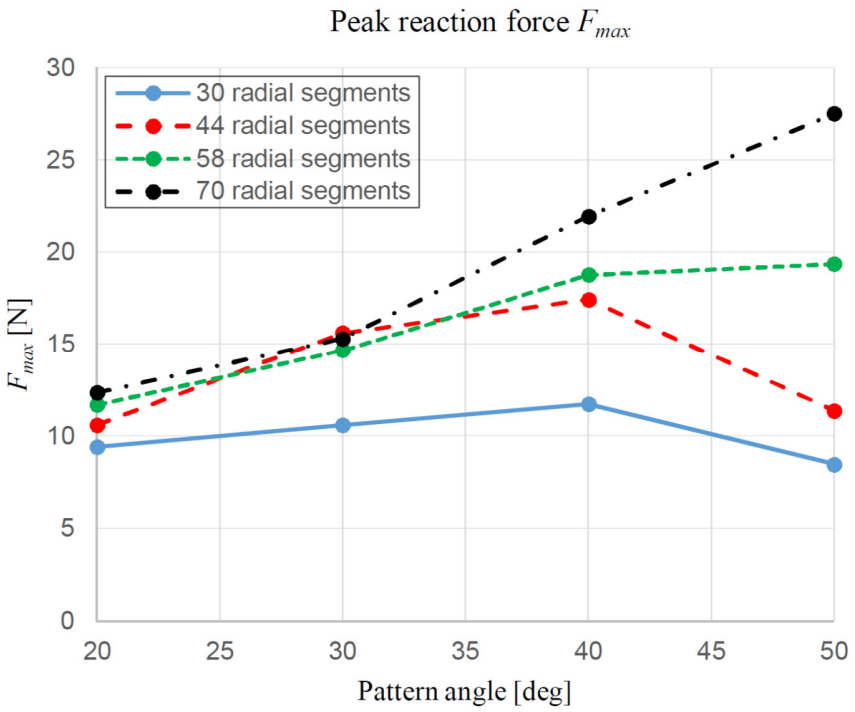

Fig. S9. Peak reaction force for each model in the parametric matrix

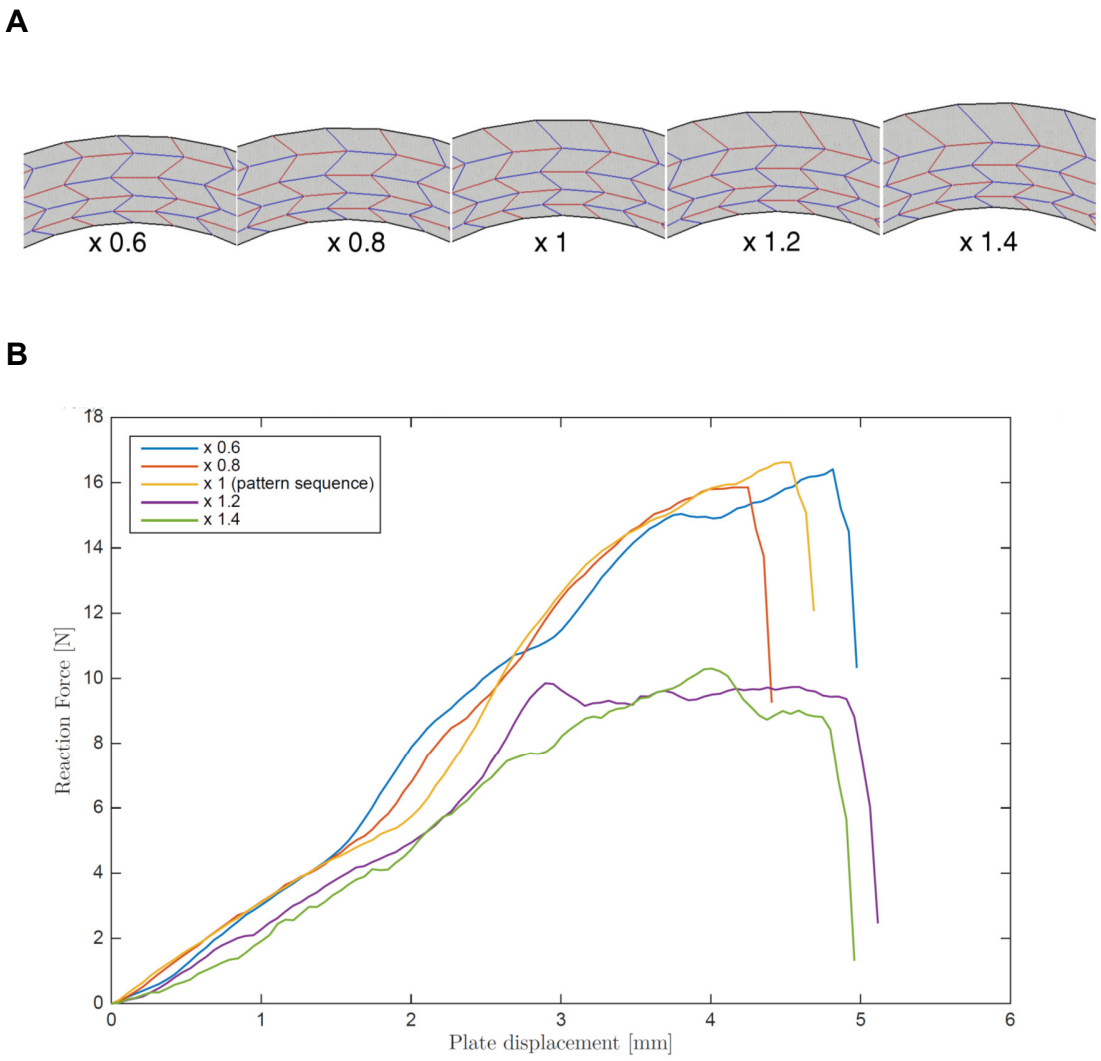

Fig. S10. Effect of the width of the most external facets (parameter *E*). (A) Array of models with external facet of varying width. (B) Numerical output of reference model with varying external facet width.

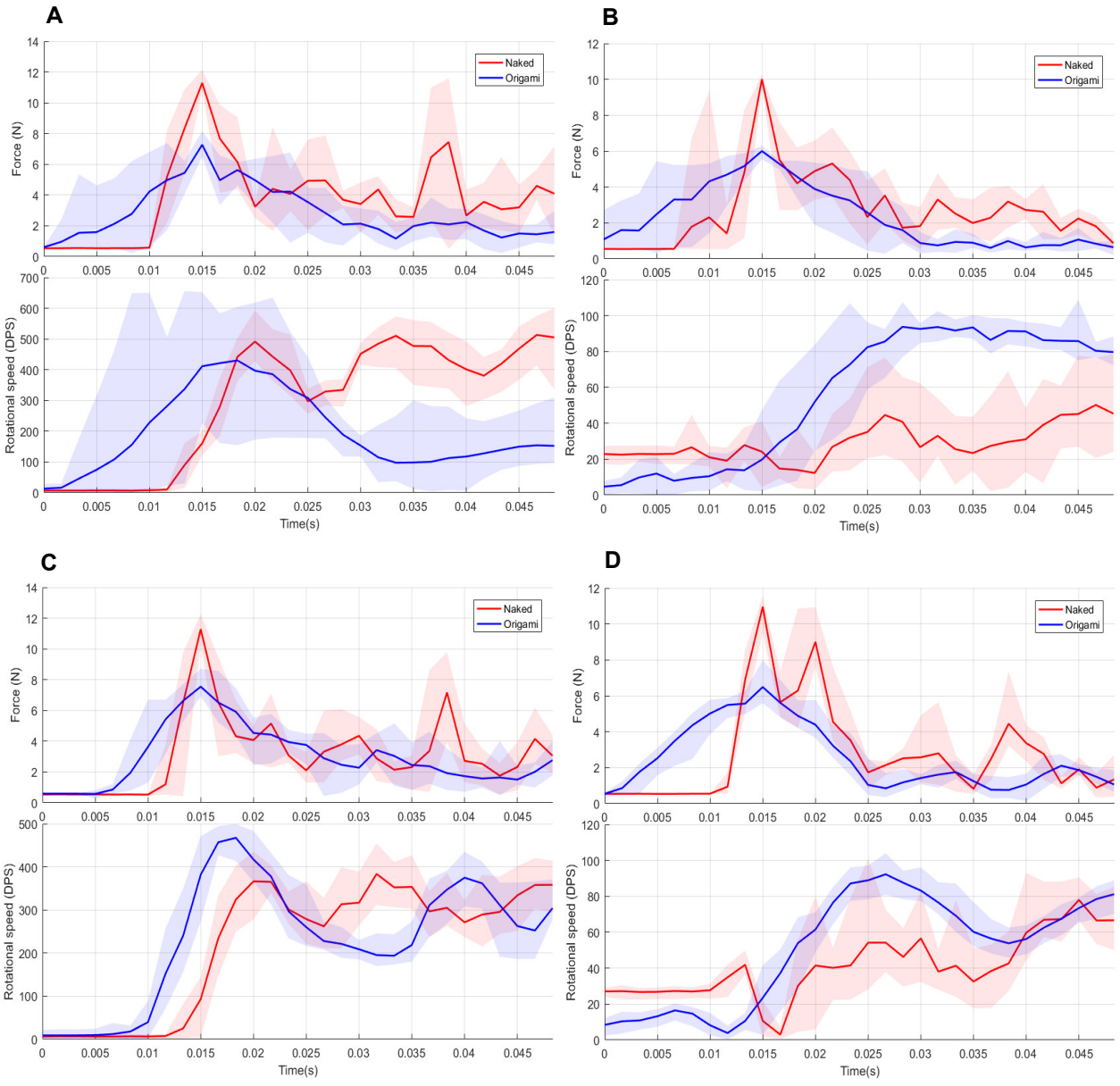

Fig. S11. Force and angular speed profiles at contact angle 60° for naked and origami protected configuration on rough and smooth surfaces. (A) Impact on rough surface with fixed protector. (B) Impact on rough surface with rotary protector. (C) Impact on smooth surface with fixed protector. (D) Impact on smooth surface with rotary protector.

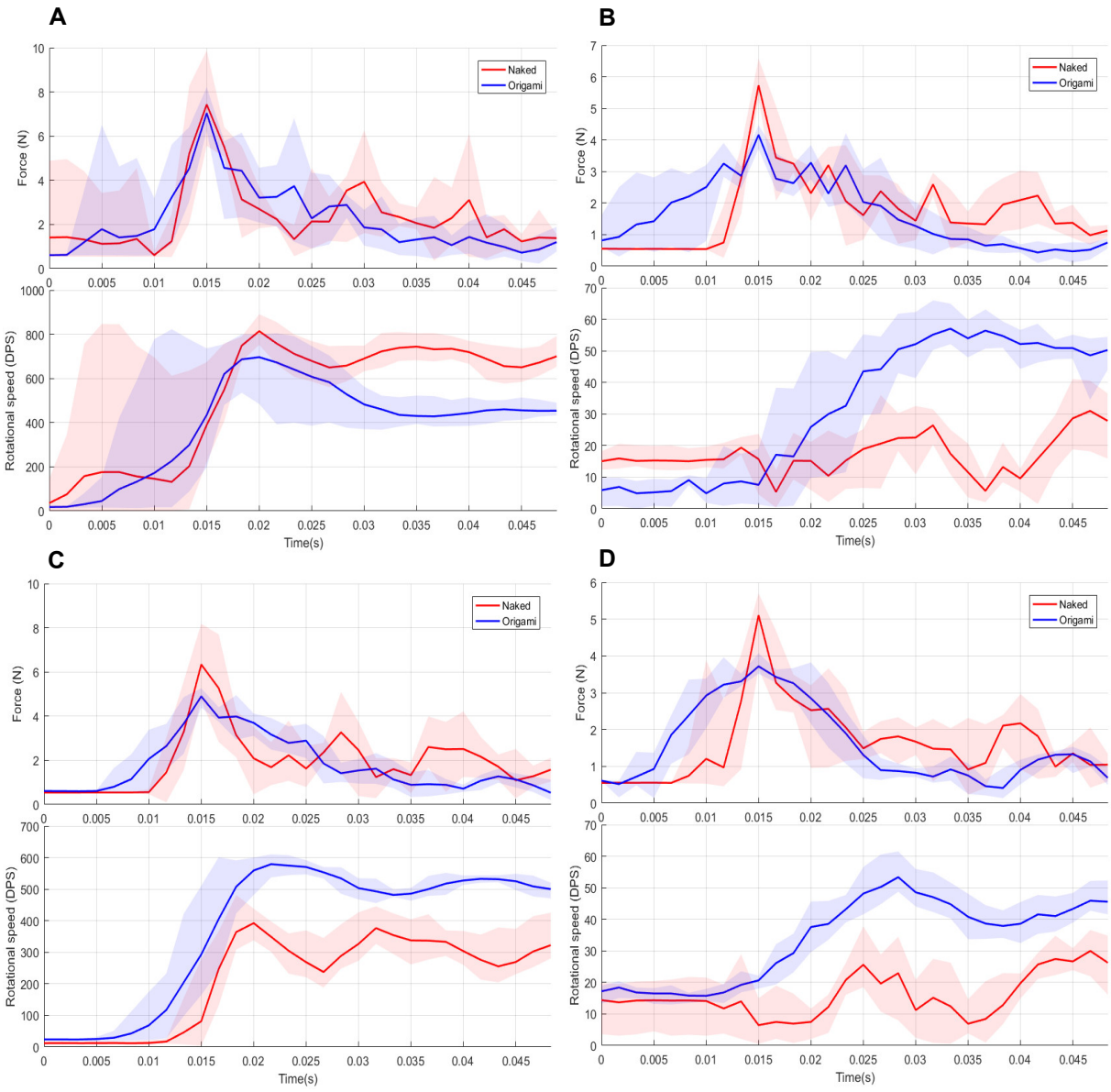

Fig. S12. Force and angular speed profiles at contact angle 30° for naked and origami protected configuration on rough and smooth surfaces. (A) Impact on rough surface with fixed protector. (B) Impact on rough surface with rotary protector. (C) Impact on smooth surface with fixed protector. (D) Impact on smooth surface with rotary protector.

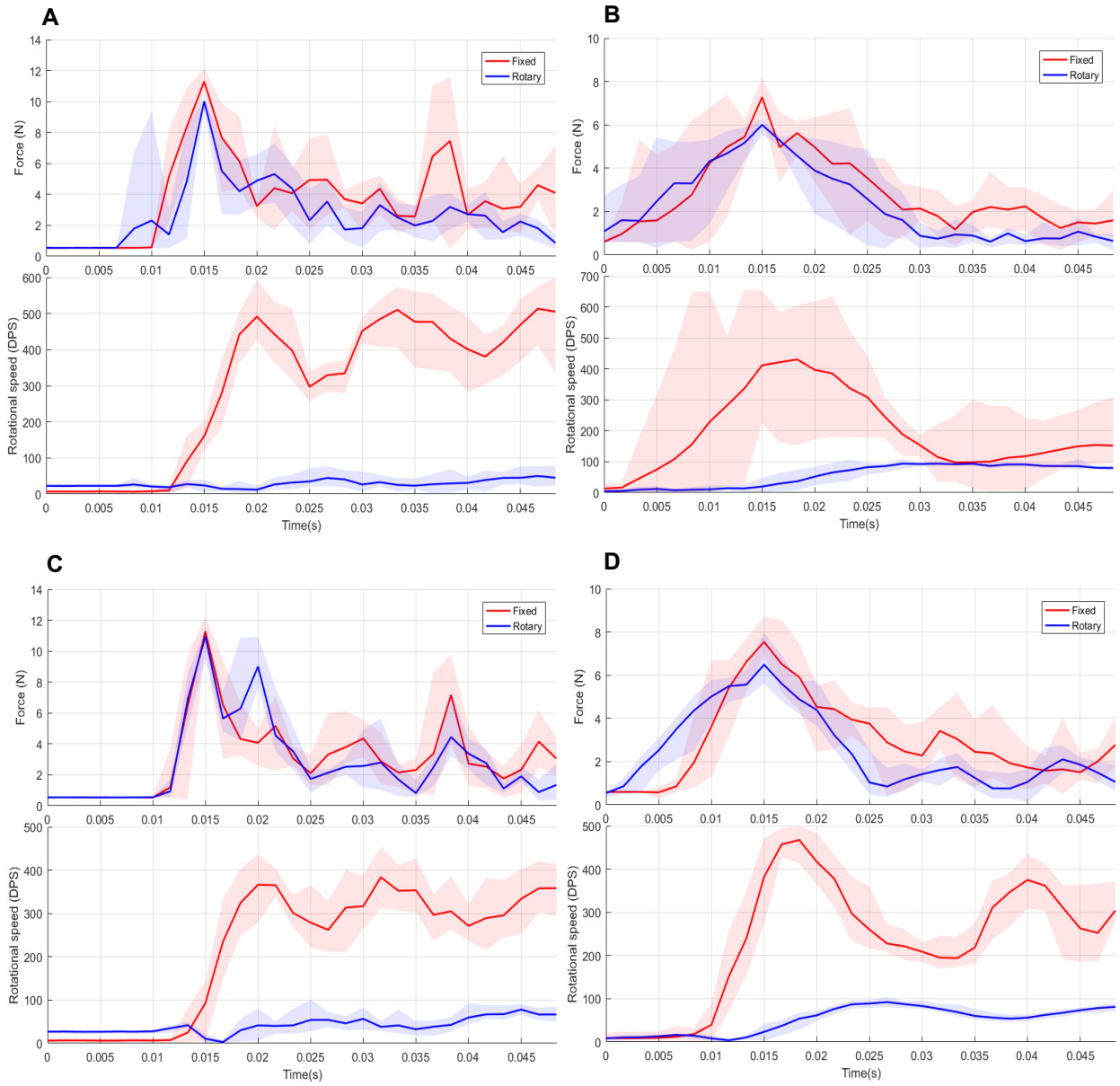

Fig. S13. Force and angular speed profiles at contact angle 60° for fixed and rotary configuration on rough and smooth surfaces. (A) Impact on rough surface with naked protector. (B) Impact on rough surface with origami protector. (C) Impact on smooth surface with naked protector. (D) Impact on smooth surface with origami protector.

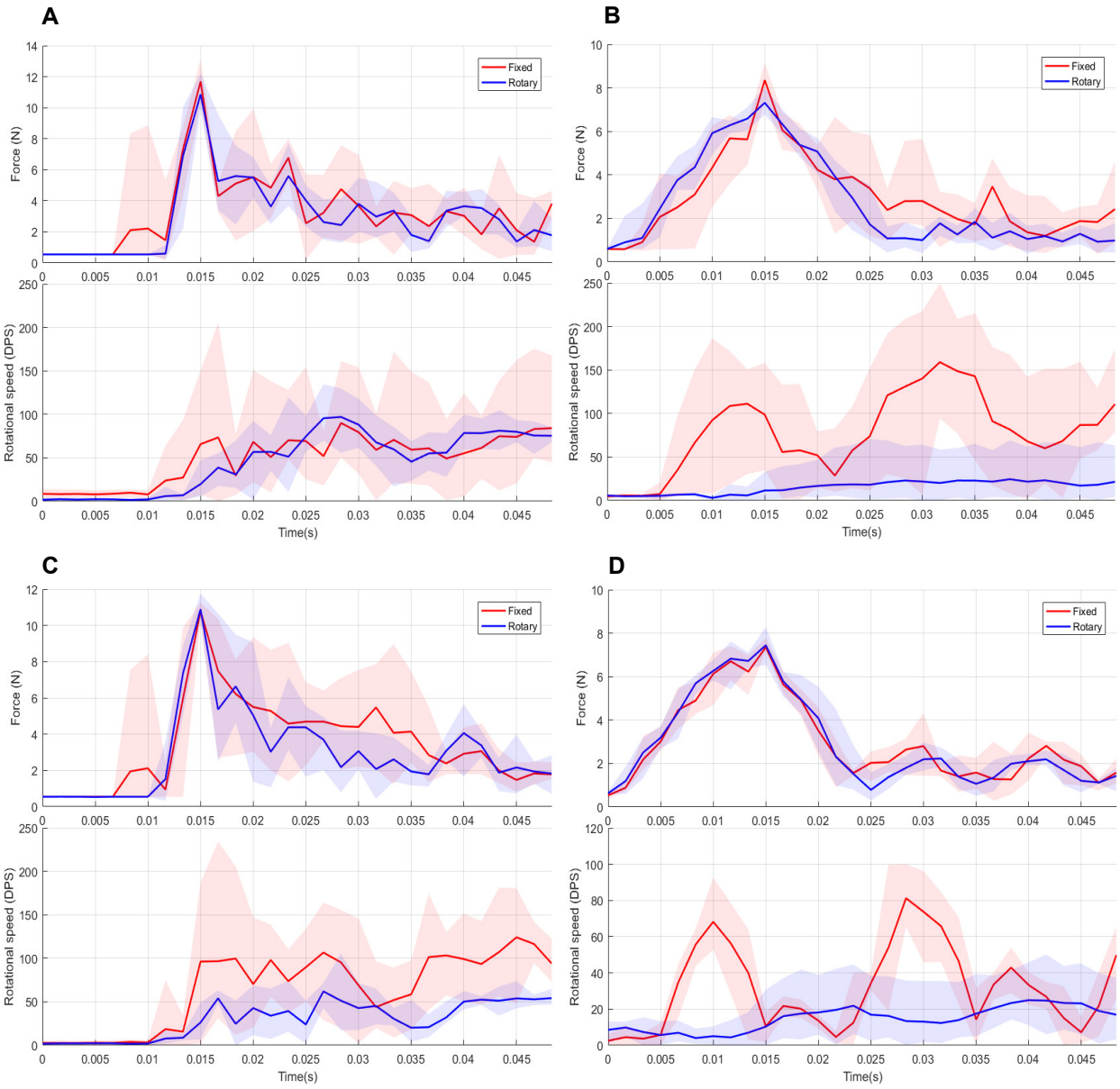

Fig. S14. Force and angular speed profiles at contact angle 90° for fixed and rotary configuration on rough and smooth surfaces. (A) Impact on rough surface with naked protector. (B) Impact on rough surface with origami protector. (C) Impact on smooth surface with naked protector. (D) Impact on smooth surface with origami protector.

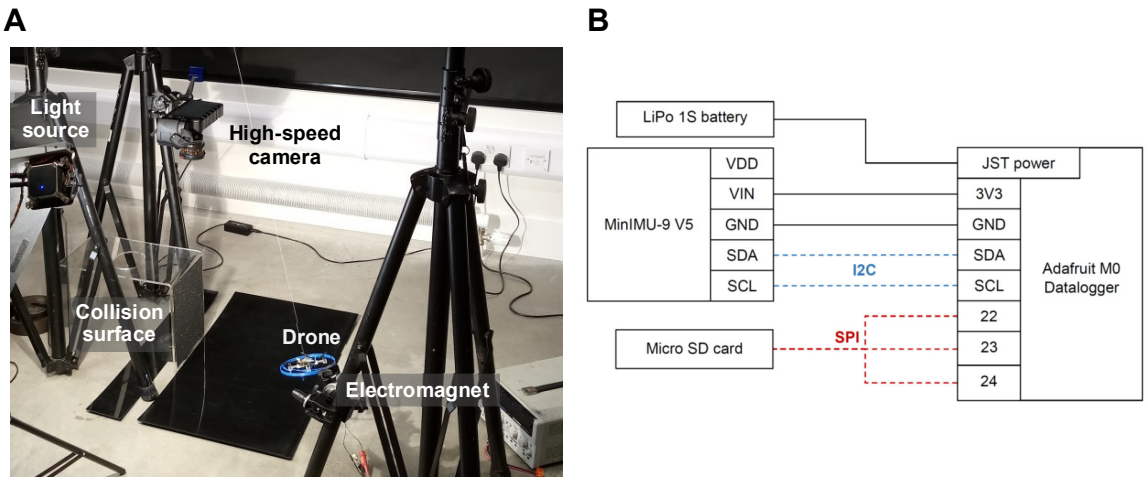

Fig. S15. (A) Experimental setup for pendulum collision tests of a miniature quadcopter to a surface. (B) Connection between MinIMU-9 V5 and Adafruit Feather M0 data logger.

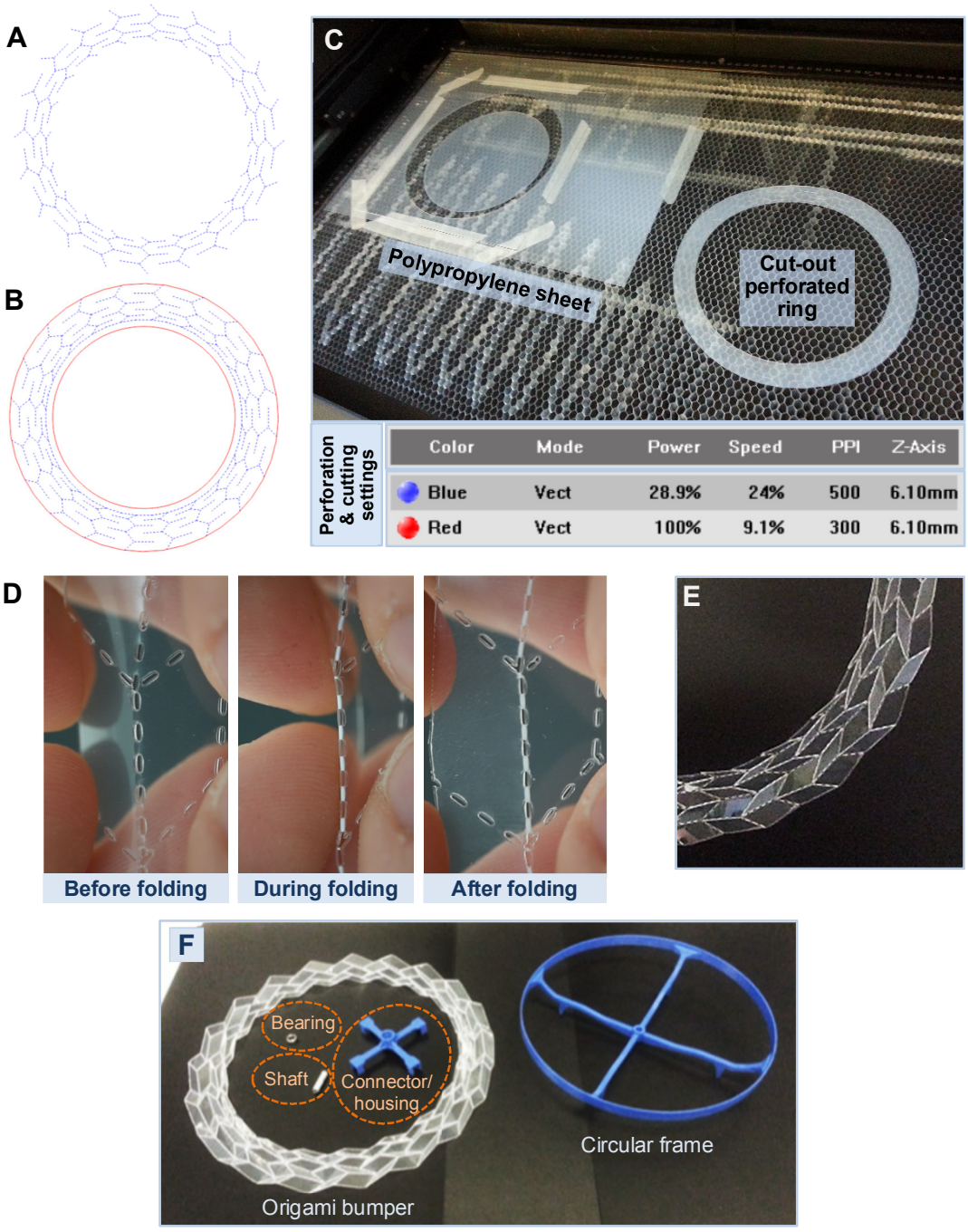

Fig. S16. (A) Drawing for mountain fold lines perforations (blue). (B) Drawing for valley fold lines perforations (blue) and the borders of the ring to be cut (red). (C) Laser perforation and cutting of the origami pattern from a polypropylene sheet (including perforation and cutting settings). (D) Manual folding process of the perforated pattern with plastic deformation along the fold lines during fabrication. (E) A quarter of the pattern folded manually. (F) Components of the rotary origami protective system including the circular frame (ABS), connector/bearing housing (ABS), shaft (aluminum), bearing (steel), and origami bumper (polypropylene).

Table S1. Summary of experimental results

Collision scenario				Experimental outputs		Improvement %	
Collision angle	Surface type	Impact cushion	Rotational DOF	Avg. peak force (N)	Avg. peak angular speed (DPS)	Average peak force	Average peak angular speed
30°	Rough	Naked	Fixed	7.43	814.26	0.00	0.00
			Rotary	5.73	30.98	22.92	96.20
		Origami	Fixed	7.04	696.50	5.26	14.46
			Rotary	4.16	57.02	44.02	93.00
	Smooth	Naked	Fixed	6.34	392.37	0.00	0.00
			Rotary	5.11	29.97	19.47	92.36
		Origami	Fixed	4.90	579.22	22.77	-47.62
			Rotary	3.72	53.37	41.35	86.40
60°	Rough	Naked	Fixed	11.29	513.21	0.00	0.00
			Rotary	10.01	50.23	11.38	90.21
		Origami	Fixed	7.27	430.29	35.61	16.16
			Rotary	6.00	93.75	46.84	81.73
	Smooth	Naked	Fixed	11.28	383.67	0.00	0.00
			Rotary	10.96	77.97	2.87	79.68
		Origami	Fixed	7.55	467.42	33.08	-21.83
			Rotary	6.49	92.29	42.46	75.95
90°	Rough	Naked	Fixed	11.69	90.04	0.00	0.00
			Rotary	10.86	97.02	7.12	-7.75
		Origami	Fixed	8.35	159.05	28.55	-76.64
			Rotary	7.31	24.45	37.44	72.84
	Smooth	Naked	Fixed	10.79	124.11	0.00	0.00
			Rotary	10.90	61.90	-0.99	50.12
		Origami	Fixed	7.35	81.27	31.87	34.51
			Rotary	7.44	24.93	31.01	79.92

Table S2. Control registers for the IMU

Control register	Value (Hex)	Value (Binary)	Description
CTRL1_XL	0x74	0b01110100	Accelerometer range = ±16g, data rate = 833 Hz, AAF = 400Hz
CTRL2_G	0x7C	0b01111100	Rotational velocity range = 2000 DPS, data rate = 833 Hz

Movie S1

Oblique collision to a rough surface at contact angle 30º for the origami-protected and naked systems in the fixed and rotary configurations at 1.2 m/s (0.03x).

Movie S2

Oblique collision to a rough surface at contact angle 60º for the origami-protected and naked systems in the fixed and rotary configurations at 1.2 m/s (0.03x).

Movie S3

Normal collision to a rough surface for the origami-protected and naked systems in the fixed and rotary configurations at 1.2 m/s (0.03x).

Movie S4

Normal collision to a rough surface for the origami-protected system in the fixed and rotary configurations at 2 m/s (0.03x), and collisions of the aerial vehicle in the Rotorigami configuration with different obstacles during flight demonstrations.